

Polarization and fundamental sensitivity of ^{39}K (^{133}Cs)- ^{85}Rb - ^{21}Ne co-magnetometers

Jian-Hua Liu^{1,3}, Dong-Yang Jing^{1,2}, Lin Zhuang⁴, Wei Quan^{†,5}, Jiancheng Fang⁵, Wu-Ming Liu^{†,1,2}

The hybrid optical pumping spin exchange relaxation free (HOPSERF) atomic co-magnetometers makes ultrahigh sensitivity measurement of inertia be achievable. The wall relaxation rate has a big effect on the polarization and fundamental sensitivity for the co-magnetometer, but it is often neglected in the experiments. However, there is almost no work about the systematic analysis of the influence factors on the polarization and the fundamental sensitivity of the HOPSERF co-magnetometers. Here, we systematically studied the polarization and the fundamental sensitivity of ^{39}K - ^{85}Rb - ^{21}Ne and ^{133}Cs - ^{85}Rb - ^{21}Ne HOPSERF co-magnetometers with low polarization limit and the wall relaxation rate. The ^{21}Ne number density, the photon number flux, the pump beam spot radius and frequency rate will affect the polarization greatly by affecting the the pumping rate of pump beam. We obtain a general formula on the fundamental sensitivity of the HOPSERF co-magnetometers due to shot-noise and the fundamental sensitivity changes with multiple systemic parameters, where the suitable number density of buffer gas and quench gas make the fundamental sensitivity highest. The fundamental sensitivity 7.5878×10^{-11} rad/s/Hz^{1/2} of ^{133}Cs - ^{85}Rb - ^{21}Ne co-magnetometer is higher than the ultimate theoretical sensitivity 2×10^{-10} rad/s/Hz^{1/2} of K - ^{21}Ne co-magnetometer. The fundamental sensitivity limit of ^{133}Cs - ^{85}Rb - ^{21}Ne co-magnetometer is superior to 3.7334×10^{-12} rad/s/Hz^{1/2}.

¹Beijing National Laboratory for Condensed Matter Physics, Institute of Physics, Chinese

Academy of Sciences, Beijing 100190, China

²*School of Physical Sciences, University of Chinese Academy of Sciences, Beijing 100190, China*

³ *School of Science, Beijing Technology and Business University, Beijing 100048, China*

⁴ *School of Physics, Sun Yat-Sen University, Guangzhou 510275, China*

⁵*School of Instrument Science and Opto-Electronics Engineering, and Science and Technology on Inertial Laboratory, Beihang University, Beijing 100191, China*

†*e-mail: wliu@iphy.ac.cn, quanwei@buaa.edu.cn*

In recent years, ultrahigh sensitive co-magnetometers have become a hotspot in research of inertial navigation, geophysics ^{1,2}, gravitational wave detection ³, downhole orientation sensing ⁴ and general relativity test ⁵. The representative traditional mechanical gyroscope based on electrostatic suspended rotators ⁵ is still the highest precision gyroscope on Earth. The ring laser gyroscope and the fiber optic gyroscope based on the Sagnac effect are widely used in sea and space navigation ⁶. With the rapid development of quantum physics, the spin exchange relaxation free (SERF) atomic spin co-magnetometer ⁷ uses hyperpolarized nuclear spins to sense rotation. Research on the atomic co-magnetometers contributes to the development of more wide variety of rotation sensing techniques. The simple arrangement and small volume of the co-magnetometer will ensure its wide application in the field of inertial navigation. Atomic co-magnetometers ^{8,9} use two or more spin species with different gyromagnetic ratios occupying the same volume to cancel the sensitivity of the co-magnetometers to random changing magnetic field and this leaves them only sensitive to rotation or other fields.

Atomic co-magnetometers also find applications in other precision measurement experiments: searches for violation of local Lorentz invariance ^{10,11}, studies spin-dependent forces ¹²⁻¹⁵ and searches for electric dipole moments ¹⁶. A SERF atomic co-magnetometer based on K-³He ¹⁷ reached rotation sensitivity of 5×10^{-7} rad/s/Hz^{1/2} in 2005. A Cs-¹²⁹Xe co-magnetometer was also studied ¹⁸. Due to the formation of van der Waals molecules between Cs and ¹²⁹Xe ¹⁹, the Cs relaxation rate is much larger than that of the Rb in a Rb-²¹Ne pair. A K-Rb-²¹Ne co-magnetometer guarantees high sensitivity for rotation sensing. Theoretical analysis shows that the fundamental rotation sensitivity ¹⁷ of a K-²¹Ne atomic co-magnetometer could reach 2×10^{-10} rad/s/Hz^{1/2} with 10 cm³ sense volume as the density of K is 1×10^{14} cm⁻³, the number density of buffer gas ²¹Ne is 6×10^{19} cm⁻³. A dual-axis K-Rb-²¹Ne comagnetometer can suppress the cross-talk effect and carry out high-precision rotation sensing along two sensitive axes simultaneously and independently ²⁰ and a parametrically modulated dual-axis Cs-Rb-Ne atomic spin gyroscope can effectively suppress low frequency drift and achieve a bias instability of less than 0.05 deg/h ²¹.

It was found that HOP can make the SERF magnetometer realize higher experimental detecting sensitivity and more homogeneous atomic spin polarization ²², it is suitable for quantum nondestructive measurement ²³ and HOP is also helpful for co-magnetometer to realize ultrahigh sensitivity measurement of inertia. There need more practical methods to obtain higher fundamental sensitivity of the co-magnetometer.

In this report, we studied the polarization and fundamental sensitivity of the HOPSERF co-magnetometer, take the wall relaxation rate into account, which has a big effect on the po-

larization and fundamental sensitivity, but a lot of time it is neglected in the experiments. We obtain a general formula on the fundamental sensitivity with a low polarization limit, which describes the fundamental sensitivity of the co-magnetometer changing with the number density of buffer gas and quench gas, frequency rate of pump beam, photon number flux, mole fraction of ^{85}Rb , power density of pump beam, external magnetic field, cell effective radius (the shape of the cell is roughly spherical), the pump beam spot radius, measurement volume, cell temperature and measurement time. We have investigated ^{39}K - ^{85}Rb - ^{21}Ne and ^{133}Cs - ^{85}Rb - ^{21}Ne HOPSERF atomic magnetometers (^{39}K (^{133}Cs)- ^{85}Rb - ^{21}Ne co-magnetometers), then found the fundamental sensitivity of ^{133}Cs - ^{85}Rb - ^{21}Ne co-magnetometer is higher than the one of ^{39}K - ^{85}Rb - ^{21}Ne co-magnetometers at the same cell temperature and in the SERF regime when the frequency rate of pump beam is bigger than about 3.3632×10^{14} Hz or smaller than about 3.3437×10^{14} Hz or the external magnetic field is smaller than about 2.0182×10^{-8} T, or the mole fraction of ^{85}Rb is bigger than about a critical value 0.9650 in our chosen conditions. Optimizing the co-magnetometer parameters is advantageous to improve the sensitivity of the co-magnetometer in measuring weak rotation signal.

Furthermore, we obtained a higher fundamental sensitivity of 7.5878×10^{-11} rad/s/Hz $^{1/2}$ with ^{133}Cs - ^{85}Rb - ^{21}Ne co-magnetometer when the polarization of ^{85}Rb atom is 8.5627×10^{-8} , the measurement time is 1s, cell temperature is 407.098 K, the number density of Rb is 1×10^{14} cm $^{-3}$, cell effective radius $a = 2$ cm, measurement volume is 10 cm 3 , external magnetic field $B = 1 \times 10^{-15}$ T, the number density of quench gas N_2 is 1×10^{19} cm $^{-3}$, the number density of buffer gas ^{21}Ne is 6×10^{19} cm $^{-3}$ and the fundamental sensitivity is higher than the fundamental rotation sensitivity¹⁷ of a K- ^{21}Ne atomic co-magnetometer of 2×10^{-10} rad/s/Hz $^{1/2}$. These

findings not only optimize the parameters for the SERF regime, but also provide an experimental guide for the design of the SERF co-magnetometers.

Results

The number density of alkali-metal atoms. The SERF atomic co-magnetometers have some similar properties with the SERF atomic magnetometers. As we have discussed in our previous work ²⁴, we take the alkali metal vapor cell (the shape of the cell is roughly spherical) of the SERF atomic co-magnetometers based on HOP contain two types of alkali metal atoms, ³⁹K-⁸⁵Rb or ¹³³Cs-⁸⁵Rb, we take ³⁹K or ¹³³Cs as A respectively, select ⁸⁵Rb as B in the SERF regime.

The saturated density ²⁷ of the alkali-metal atoms vapor in units of cm^{-3} at cell temperature T in Kelvin is $n_{sat} = \frac{1}{T} 10^{21.866 + A_1 - B_1/T}$. A_1 and B_1 are phase parameters ²⁵, where $A_1^K = 4.402$, $A_1^{Rb} = 4.312$, $A_1^{Cs} = 4.165$, $B_1^K = 4453$, $B_1^{Rb} = 4040$ and $B_1^{Cs} = 3830$ for the temperature is higher than 400 K.

Because SERF regime can be reached by operating with sufficiently high alkali metal number density (at higher temperature) and in sufficiently low magnetic field ^{28,29}, as we discussed in our previous work ²⁴, we choose $T = 457.5$ K as the highest temperature to reduce the corrosion of alkali metal atoms to the vapor cell and make the co-magnetometers be in the SERF regime.

The polarization of alkali-metal atom. Considering the spin-exchange between alkali-metal atoms A and B in the hybrid vapor cell, we assume that the vapor densities obey the Raoult's

law³⁰, $n_B \approx f_B n_{sat}^B$, where f_B is the mole fraction of atom B in the metal and n_{sat}^B is the saturated vapor density for pure atom B metal. When the mole fraction of atom B is 0.97, we can obtain the number density of atom A and B, $n_A \approx 0.03n_{sat}^A$, $n_B \approx 0.97n_{sat}^B$. For K-Rb-²¹Ne atomic comagnetometer, suppose that in an alkali-metal vapor cell filled with K, Rb and ²¹Ne atoms, the density ratio of K to Rb is $D_r = n_K/n_{Rb}$ (where n_K and n_{Rb} are the number densities of K and Rb, respectively). K atom spins are directly polarized by the D_1 line light and Rb atomic spins are polarized through spin exchange with K atom spins. If the frequency rate of the laser beam ν , is tuned away from the absorption center of the pressure³¹ and the power-broadened³² D_1 absorption line, there will be an AC Stark shift of K, which is denoted as L_z^K in the light propagation direction³⁵, where the light propagation direction is in the z direction. For Rb atom spins, the far-off-resonant laser will cause an AC Stark shift L_z^{Rb} on the D_1 and D_2 line transitions of Rb atoms. K atom spins polarize Rb atom spins by the spin-exchange interaction. The spin transfer rate from Rb to K is given by $R_{Rb-K}^{SE} = n_{Rb} \sigma_{SE}^{Rb-K} \bar{v}_{Rb-K}$, where σ_{SE}^{Rb-K} is the spin-exchange cross section between Rb and K³³ and \bar{v}_{Rb-K} is the relative velocity between Rb and K. Thus the spin transfer rate from K to Rb is $R_{K-Rb}^{SE} = D_r R_{Rb-K}^{SE}$.

The full Bloch equations are given by^{34,35},

$$\begin{aligned} \frac{\partial \mathbf{P}_K^e}{\partial t} = & \frac{\gamma^e}{Q(P_K^e)} (\mathbf{B} + \mathbf{L}^K) \times \mathbf{P}_K^e \\ & + \frac{R_p s_p - R_p \mathbf{P}_K^e + R_{Rb-K}^{SE} (\mathbf{P}_{Rb}^e - \mathbf{P}_K^e)}{Q(P_K^e)}, \end{aligned} \quad (1)$$

$$\begin{aligned}
\frac{\partial \mathbf{P}_{\text{Rb}}^e}{\partial t} = & \frac{\gamma^e}{Q(P_{\text{Rb}}^e)} (\mathbf{B} + \lambda_{\text{Rb-Ne}} M_0^n \mathbf{P}^n + \mathbf{L}^{\text{Rb}}) \times \mathbf{P}_{\text{Rb}}^e \\
& + \frac{D_r R_{\text{Rb-K}}^{\text{SE}} (\mathbf{P}_{\text{K}}^e - \mathbf{P}_{\text{Rb}}^e)}{Q(P_{\text{Rb}}^e)} \\
& - \frac{1}{T_{2e}, T_{2e}, T_{1e}} \frac{\mathbf{P}_{\text{Rb}}^e}{Q(P_{\text{Rb}}^e)}, \tag{2}
\end{aligned}$$

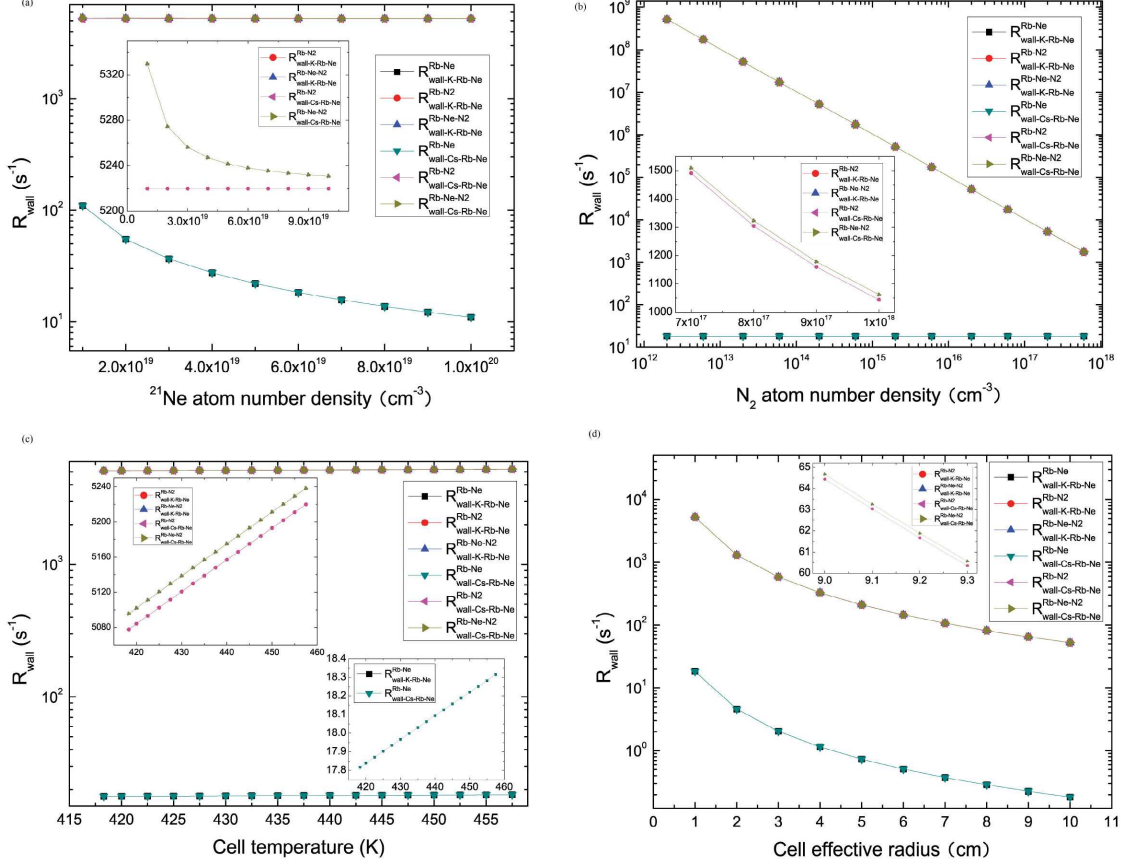
$$\begin{aligned}
\frac{\partial \mathbf{P}^n}{\partial t} = & \gamma^n (\mathbf{B} + \lambda_{\text{Rb-Ne}} M_0^{\text{Rb}} \mathbf{P}_{\text{Rb}}^e) \times \mathbf{P}^n \\
& + \boldsymbol{\Omega} \times \mathbf{P}^n + R_{\text{Rb-Ne}}^{\text{se}} (\mathbf{P}_{\text{Rb}}^e - \mathbf{P}^n) \\
& - \frac{1}{T_{2n}, T_{2n}, T_{1n}} \mathbf{P}^n, \tag{3}
\end{aligned}$$

where \mathbf{P}_{K}^e , \mathbf{P}_{Rb}^e and \mathbf{P}^n are the polarizations of K, Rb and ^{21}Ne atom spins, respectively, and $\boldsymbol{\Omega}$ is the input rotation velocity. $Q(P_{\text{K}}^e)$ and $Q(P_{\text{Rb}}^e)$ is the slow-down factor caused by the rapid spin exchange³⁶. It is related to the nuclear spin moment and the K and Rb spins should have different slow-down factors. However, the rapid spin exchange between the K and Rb spins can change the slow-down factors of both K and Rb atom spins. The slow-down factors will be the same when they involve collision with each other³⁵. B is the external magnetic field. L^{K} and L^{Rb} are the AC Stark shifts of the K atoms and Rb atoms respectively by the laser beam. R_p is the pumping rate of K atoms (or the pumping rate of Cs atoms for the SERF atomic co-magnetometers based on ^{133}Cs - ^{85}Rb), which is mainly determined by pumping laser parameters¹⁷, while s_p gives the direction and magnitude of photon spin polarization. $R_{\text{Rb-K}}^{\text{SE}}$ is the spin-exchange transfer rate from Rb atoms to K atoms. $\lambda_{\text{Rb-Ne}} M_0^n \mathbf{P}^n$ is the magnetic field produced by the ^{21}Ne atom spins through spin-exchange interaction with Rb atom spins³⁷. $\lambda_{\text{Rb-Ne}} = 8\pi\kappa_{\text{Rb-Ne}}/3$, where $\kappa_{\text{Rb-Ne}}$ is a spin-exchange enhancement factor resulting from the overlap of the Rb electron wave function with the ^{21}Ne nucleus and is approximately 35.7 for Rb- ^{21}Ne pair³⁸. $M_0^n = \mu_{\text{Ne}} n_{\text{Ne}}$, where μ_{Ne} is nuclear

magnetic moment and n_{Ne} is ^{21}Ne atom number density. Rb atom spins also produce a magnetic field $\lambda_{Rb-Ne} M_0^{Rb} \mathbf{P}_{Rb}^e$, which is experienced by the ^{21}Ne spins. $1/T_{2e}$ and $1/T_{1e}$ are the transverse and longitude relaxation rates of Rb atom spins respectively. $1/T_{1e} = R_{SD}^{Rb} + D_r R_p + R_{Wall}^{Rb}$, $R_{SD}^{Rb} = n_{Rb} \sigma_{SD}^{Rb-Rb} \bar{v}_{Rb-Rb} + n_{Ne} \sigma_{SD}^{Rb-Ne} \bar{v}_{Rb-Ne} + n_{N_2} \sigma_{SD}^{Rb-N_2} \bar{v}_{Rb-N_2} + n_{Rb} \sigma_{SD}^{Rb-K} \bar{v}_{Rb-K}$. R_{Wall}^{Rb} is the relaxation rates due to diffusion of Rb atom to the wall (the wall relaxation of Rb atoms)¹⁷, $R_{Wall}^{Rb} = Q(P_{Rb}^e) D_{Ne}^{Rb} \left(\frac{\sqrt{1+T/273.15}}{P_{Ne}/1\text{amg}} \right) \left(\frac{\pi}{a} \right)^2 + Q(P_{Rb}^e) D_{N_2}^{Rb} \left(\frac{\sqrt{1+T/273.15}}{P_{N_2}/1\text{amg}} \right) \left(\frac{\pi}{a} \right)^2$, D_{Ne}^{Rb} is the diffusion constant of the alkali atom Rb within the buffer gas Ne³⁹⁻⁴¹ in units of cm^2/s and is given at 1 amg and 273 K, $D_{N_2}^{Rb}$ is the diffusion constant of the alkali atom Rb within the quench gas N_2 ⁴⁰⁻⁴² in units of cm^2/s and is given at 1 amg and 273 K, $1\text{amg} = 2.69 \times 10^{19} \text{ cm}^{-3}$, $D_{Ne}^{Rb} = 0.2 \text{ cm}^2/\text{s}$, $D_{N_2}^{Rb} = 0.19 \text{ cm}^2/\text{s}$, P_{Ne} is the pressure intensity of buffer gas Ne in amg, P_{N_2} is the pressure intensity of quench gas N_2 in amg, a is the equivalent radius of vapor cell.

The transverse relaxation rate of Rb atom spins comes from the spin-exchange relaxation rate of Rb atoms^{43,44} $Q(P_{Rb}^e)/T_2^{SE}$, and $1/T_{1e}$, $1/T_{2e} = 1/T_{1e} + Q(P_{Rb}^e)/T_2^{SE}$. R_{Rb-Ne}^{se} is the spin-exchange transfer rate from Rb to ^{21}Ne atom spins. $1/T_{2n}$ and $1/T_{1n}$ are the transverse and longitude relaxation rates of the ^{21}Ne atom spins respectively. The AC Stark shift of Rb atom spins is measured by measuring the polarization of Rb atom spins along the x direction P_{xRb}^e , with a probe laser whose wavelength is tuned to the Rb D_1 line. After hours of spin-exchange optical pumping of the ^{21}Ne spins, the polarization of ^{21}Ne will reach steady state. Suppose that a B_z magnetic field is applied to the comagnetometer. The virtual magnetic fields of K and Rb caused by AC Stark shifts are in the z direction. At steady state, $\partial \mathbf{P}_K^e / \partial t = 0$, $\partial \mathbf{P}_{Rb}^e / \partial t = 0$ and $\partial \mathbf{P}^n / \partial t = 0$. For the low polarization limit, $R_{wall}^{Rb} = Q(0)_{Rb} D_{Ne}^{Rb} \left(\frac{\sqrt{1+T/273.15}}{P_{Ne}/1\text{amg}} \right) \left(\frac{\pi}{a} \right)^2 +$

$$Q(0)_{Rb} D_{N_2}^{Rb} \left(\frac{\sqrt{1+T/273.15}}{P_{N_2}/1\text{atm}g} \right) \left(\frac{\pi}{a} \right)^2.$$



The wall relaxation rates change with the ^{21}Ne number density n_{Ne} in Fig. 1(a), the N_2 number density n_{N_2} in Fig. 1(b), the cell temperature T in Fig. 1(c) and the cell effective radius a in Fig. 1(d), respectively. The illustration in Fig. 1(a) shows that $R_{\text{wall-K-Rb-Ne}}^{Rb-N_2}$ and $R_{\text{wall-Cs-Rb-Ne}}^{Rb-N_2}$ don't change when n_{Ne} increases, $R_{\text{wall-K-Rb-Ne}}^{Rb-Ne}$ and $R_{\text{wall-Cs-Rb-Ne}}^{Rb-Ne}$ decrease with increasing n_{Ne} , therefore, $R_{\text{wall-K-Rb-Ne}}^{Rb-Ne-N_2}$ and $R_{\text{wall-Cs-Rb-Ne}}^{Rb-Ne-N_2}$ decrease with increasing n_{Ne} . The illustration in Fig. 1(b) shows that $R_{\text{wall-K-Rb-Ne}}^{Rb-N_2}$, $R_{\text{wall-Cs-Rb-Ne}}^{Rb-N_2}$, $R_{\text{wall-K-Rb-Ne}}^{Rb-Ne-N_2}$ and $R_{\text{wall-Cs-Rb-Ne}}^{Rb-Ne-N_2}$ decrease with increasing n_{N_2} . The illustration in Fig. 1(c)

shows that $R_{wall-K-Rb-Ne}^{Rb-Ne}$, $R_{wall-Cs-Rb-Ne}^{Rb-Ne}$, $R_{wall-K-Rb-Ne}^{Rb-N_2}$, $R_{wall-Cs-Rb-Ne}^{Rb-N_2}$, $R_{wall-K-Rb-Ne}^{Rb-Ne-N_2}$ and $R_{wall-Cs-Rb-Ne}^{Rb-Ne-N_2}$ increase with the increasing T . The illustration in Fig. 1(d) shows that $R_{wall-K-Rb-Ne}^{Rb-N_2}$, $R_{wall-Cs-Rb-Ne}^{Rb-N_2}$, $R_{wall-K-Rb-Ne}^{Rb-Ne-N_2}$ and $R_{wall-Cs-Rb-Ne}^{Rb-Ne-N_2}$ decrease with increasing a , $R_{wall-K-Rb-Ne}^{Rb-Ne-N_2}$ and $R_{wall-Cs-Rb-Ne}^{Rb-Ne-N_2}$ are bigger than $R_{wall-K-Rb-Ne}^{Rb-N_2}$ and $R_{wall-Cs-Rb-Ne}^{Rb-N_2}$, respectively.

We can find that the relaxation rates for diffusion of ^{85}Rb in the ^{21}Ne gas to the wall of ^{39}K - ^{85}Rb - ^{21}Ne co-magnetometer $R_{wall-K-Rb-Ne}^{Rb-Ne}$, the total relaxation rates for diffusion of ^{85}Rb in the ^{21}Ne and N_2 gas to the wall of ^{39}K - ^{85}Rb - ^{21}Ne co-magnetometer $R_{wall-K-Rb-Ne}^{Rb-Ne-N_2}$, the relaxation rates for diffusion of ^{85}Rb in the ^{21}Ne gas to the wall of ^{133}Cs - ^{85}Rb - ^{21}Ne co-magnetometer $R_{wall-Cs-Rb-Ne}^{Rb-Ne}$ and the total relaxation rates for diffusion of ^{85}Rb in the ^{21}Ne gas to the wall of ^{133}Cs - ^{85}Rb - ^{21}Ne co-magnetometer $R_{wall-Cs-Rb-Ne}^{Rb-Ne-N_2}$ decrease when ^{21}Ne atom number density n_{Ne} increases in Fig. 1(a), because the buffer gas ^{21}Ne atom suppresses the spin relaxation caused by wall collisions. The relaxation rates for diffusion of ^{85}Rb in the N_2 gas to the wall of ^{39}K - ^{85}Rb - ^{21}Ne co-magnetometer is $R_{wall-K-Rb-Ne}^{Rb-N_2}$, the relaxation rates for diffusion of ^{85}Rb in the N_2 gas to the wall of ^{133}Cs - ^{85}Rb - ^{21}Ne co-magnetometer is $R_{wall-Cs-Rb-Ne}^{Rb-N_2}$, $R_{wall-K-Rb-Ne}^{Rb-N_2}$, $R_{wall-K-Rb-Ne}^{Rb-Ne-N_2}$, $R_{wall-Cs-Rb-Ne}^{Rb-N_2}$ and $R_{wall-Cs-Rb-Ne}^{Rb-Ne-N_2}$ decrease when n_{N_2} increases for N_2 gas colliding with excited alkali metal atoms and absorbing the energy, which restrains radiative deexcitation of the excited alkali metal atom, $R_{wall-K-Rb-Ne}^{Rb-Ne}$ and $R_{wall-Cs-Rb-Ne}^{Rb-Ne}$ don't change when n_{N_2} increases for they are not related with n_{N_2} in Fig. 1(b).

$$R_{wall-K-Rb-Ne}^{Rb-N_2}, R_{wall-K-Rb-Ne}^{Rb-Ne-N_2}, R_{wall-Cs-Rb-Ne}^{Rb-N_2}, R_{wall-Cs-Rb-Ne}^{Rb-Ne-N_2}, R_{wall-K-Rb-Ne}^{Rb-Ne} \text{ and } R_{wall-Cs-Rb-Ne}^{Rb-Ne}$$

increase with increasing cell temperature T in Fig. 1(c) for the increasing T makes the number density and relative velocity of ^{85}Rb atoms bigger and more ^{85}Rb atoms moving towards the wall. $R_{wall-K-Rb-Ne}^{Rb-Ne}$, $R_{wall-K-Rb-Ne}^{Rb-N_2}$, $R_{wall-K-Rb-Ne}^{Rb-Ne-N_2}$, $R_{wall-Cs-Rb-Ne}^{Rb-Ne}$, $R_{wall-Cs-Rb-Ne}^{Rb-N_2}$ and $R_{wall-Cs-Rb-Ne}^{Rb-Ne-N_2}$ decreases when the cell effective radius a increases in Fig. 1(d) for the ^{85}Rb atoms colliding more ^{21}Ne atoms and N_2 atoms with the increasing a when ^{85}Rb atoms move towards the wall, which will decrease the wall relaxation rate.

The polarization in the z direction could be calculated to be $\mathbf{P}_{z\text{K}}^e \approx \mathbf{P}_{z\text{Rb}}^e \approx D_r R_p / [D_r R_p + R_{SD}^{Rb} + Q(0)_{Rb} / T_{1e}]$ ($R_p \ll R_{Rb-K}^{SE}$, $D_r \ll 1$), $\mathbf{P}_z^n \approx R_{Rb-Ne}^{se} / (R_{Rb-Ne}^{se} + 1/T_{1n})$. The angle between the spins polarization and the z direction is small by applying a small magnetic field B_y and the polarization of K, Rb and ^{21}Ne are approximately constant in the z direction, then the coupled Bloch equations can be simplified³⁵. In the x direction, the polarizations of K and Rb can be solved and are given by³⁵

$$\begin{aligned} \mathbf{P}_{x\text{K}}^e &\approx \mathbf{P}_{x\text{Rb}}^e \\ &\approx \mathbf{P}_{z\text{Rb}}^e \frac{R_{tot}^{Rb} / \gamma^e \left(\frac{B_y}{B^n} \delta B_z + \frac{\Omega_y}{\gamma^n} + \frac{L_z}{R_{tot}^{Rb} / \gamma^e} \frac{\Omega_x}{\gamma^n} \right)}{(R_{tot}^{Rb} / \gamma^e)^2 + (\delta B_z + L_z)^2}. \end{aligned} \quad (4)$$

where

$$\begin{aligned}
\mathbf{P}_{z\text{Rb}}^e &\approx \frac{D_r R_p}{D_r R_p + R_{SD}^{Rb} + Q(0)_{\text{Rb}}/T_{1e}}, \\
\frac{1}{T_{1e}} &= R_{SD}^{Rb} + D_r R_p + R_{wall}^{Rb}, \\
R_p &= R_p^K \text{ or } R_p^{Cs}, \\
R_p^K &= \frac{\Phi_{D1}^K r_e c f_{D1}^K}{A_t} \frac{\Gamma_{D1}^K/2}{(\nu - v_{0D1}^K)^2 + (\Gamma_{D1}^K/2)^2}, \\
R_p^{Cs} &= \frac{\Phi_{D1}^{Cs} r_e c f_{D1}^{Cs}}{A_t} \frac{\Gamma_{D1}^{Cs}/2}{(\nu - v_{0D1}^{Cs})^2 + (\Gamma_{D1}^{Cs}/2)^2}, \\
\delta B_z &= B_z - B^e - B^n, \\
B^n &\approx \frac{8}{3} \pi \mu_0 \kappa_{\text{Rb-Ne}} \mu_{\text{Ne}} n_{\text{Ne}} \frac{R_{\text{Rb-Ne}}^{se}}{R_{\text{Rb-Ne}}^{se} + 1/T_{1n}}, \\
B^e &= \frac{8}{3} \pi \mu_0 \kappa_{\text{Rb-Ne}} M_0^{Rb} \mathbf{P}_{z\text{Rb}}^e, \quad M_0^{Rb} \approx \mu_B n_{\text{Rb}}, \\
L_z &= D_r L_z^K + L_z^{Rb}, \\
L_z^K &= \frac{\Phi_{D1}^K r_e c f_{D1}^K}{A_t \gamma^e} \frac{\nu - v_{0D1}^K}{(\nu - v_{0D1}^K)^2 + (\Gamma_{D1}^K/2)^2}, \\
\Gamma_{D1}^K &= \Gamma_{P-D1}^K \sqrt{1 + \frac{3\lambda^3 I_{PI}^K}{\pi h c \Gamma_{P-D1}^K}}, \\
L_z^{Rb} &= \frac{\Phi_{D1}^K r_e c f_{D1}^{Rb}}{A_t \gamma^e} \left(\frac{1}{\nu - v_{0D2}^{Rb}} - \frac{1}{\nu - v_{0D1}^{Rb}} \right) \\
R_{tot}^{Rb} &= D_r R_p + R_{SD}^{Rb} + R_{wall}^{Rb} + Q(0)_{\text{Rb}}/T_2^{SE}, \\
&\quad (R_p \ll R_{\text{Rb-K}}^{SE}, D_r \ll 1)
\end{aligned}$$

the polarization of Rb spins in the x direction (Rb polarization) will be measured in the experiment, $R_{\text{Rb-Ne}}^{se} = \kappa_{\text{Rb-Ne}}^{se} n_{\text{Rb}}$, Γ_{P-D1}^K is the linewidth of the K-Ne pressure broadening, $\Gamma_{P-D1}^K = \frac{n_{\text{Ne}} P_0 T}{T_0 \times 2.69 \times 10^{19} / \text{cm}^3} \times 7.8 \text{ GHz/atm}$, $P_0 = 101.325 \text{ kPa} = 1 \text{ atm}$, $T_0 = 273.15 \text{ K}$, the linewidth of the Cs-Ne pressure broadening $\Gamma_{P-D1}^{Cs} = \frac{n_{\text{Ne}} P_0 T}{T_0 \times 2.69 \times 10^{19} / \text{cm}^3} \times 8.2 \text{ GHz/atm}$ ⁴⁵, $\mu_0 = 4\pi \times 10^{-7} \text{ T} \cdot \text{m/A}$,

$\kappa_{Rb-Ne} \approx 35.7$, $\mu_B = 9.27408 \times 10^{-24}$ J/T, $\kappa_{Rb-Ne}^{se} = \sigma_{SD}^{Rb-Ne} \bar{v}_{Rb-Ne}$, $\mu_{Ne} = 3.33 \times 10^{-27}$ J/T, $T_{1n} \approx 214 \times 60 \times 2.69 \times 10^{19} / n_{Ne}^{38}$, I_{PI}^K is the power density of pump beam, the ^{21}Ne relaxation is dominated by the electric quadrupole interaction. During binary collisions, the interaction between the induced electric-field gradients and the nuclear quadrupole moments produce torques on the spins, thus cause relaxation ⁴⁶. $r_e = 2.817938 \times 10^{-15}$ m, the resonance transition of K λ_{0D1}^K is 770.108 nm, $\nu_{0D1}^K = c/\lambda_{0D1}^K \approx 3.895 \times 10^5$ GHz, D_1 transition of Rb and Cs in vacuum are $\lambda_{0D1}^{Rb} = 795$ nm and $\lambda_{0D1}^{Cs} = 894.6$ nm, respectively, therefore, $\nu_{0D1}^{Rb} = c/\lambda_{0D1}^{Rb} \approx 3.773 \times 10^5$ GHz, $\nu_{0D1}^{Cs} = c/\lambda_{0D1}^{Cs} \approx 3.353 \times 10^5$ GHz, D_2 transition of K and Rb in vacuum are $\lambda_{0D2}^K = 766.7$ nm and $\lambda_{0D2}^{Rb} = 780.2$ nm, respectively, $\nu_{0D2}^{Rb} = c/\lambda_{0D2}^{Rb} \approx 3.845 \times 10^5$ GHz. $f_{D1}^K = 0.324$, $f_{D1}^{Cs} = 0.347$, $f_{D1}^{Rb} = 0.332$, $f_{D2}^{Rb} = 0.668$ ⁴⁷. Φ_{D1}^K is the photon number flux and A_t is the transverse area of the pumping light, $A_t = \pi a_p^2$, r_e is the classical electron radius and c is the velocity of light, f_{D1} is the oscillator strength ⁴⁸ and γ^e is the electron gyromagnetic ratio, Γ_{D1}^K is the linewidth (full width at half maximum) of the pressure and power-broadened K D_1 absorption line ⁴⁹, and ν_{0D1}^K is the absorption center frequency rate of the absorption line. The far-off-resonant pump laser will cause an AC Stark shift of Rb atoms. δB_z is the compensation magnetic field.

For small atomic polarization, the spin precession rate is given by $\omega_0 = g\mu_B B/Q(P^e)\hbar$, which is the Larmor frequency, T_{SE} is the spin-exchange time, $1/T_{SE}^{Rb} = n_{Rb}\sigma_{SE}^{Rb-Rb}\bar{v}_{Rb-Rb}$, where σ_{SE}^{Rb-Rb} is the spin-exchange cross section between Rb and Rb and \bar{v}_{Rb-Rb} is the relative velocity between Rb and Rb. $Q(P^e)$ is the slowing-down factor for polarization and nuclear angular momentum ^{27,50}, $Q(P^e)_{85Rb} = (38 + 52P^2 + 6P^4)/(3 + 10P^2 + 3P^4)$ for ^{85}Rb atom. In this limit spin exchange contributes to transverse relaxation only in second order and vanishes for zero

magnetic field ¹⁷, $1/T_2^{SE} = \omega_0^2 T_{SE} [Q(P^e)^2 - (2I + 1)^2] Q(P^e)^2 / 2Q(P^e)^2$, for low polarization limit and small magnetic fields, spin-exchange relaxation is quadratic in the magnetic field, I is nuclear spin of the alkali-metal atoms, we consider the relaxation rate due to ⁸⁵Rb-⁸⁵Rb, ⁸⁵Rb-³⁹K spin-exchange collisions, then

$$\frac{1}{T_2^{SE}} = \left(\frac{g\mu_B B}{Q(0)_{Rb} \hbar} \right)^2 \frac{Q(0)_{Rb}^2 - (2I_{Rb} + 1)^2}{2n_{Rb} \sigma_{SE}^{Rb-Rb} \bar{v}_{Rb-Rb}} + \left(\frac{g\mu_B B}{Q(0)_{Rb} \hbar} \right)^2 \frac{Q(0)_{Rb}^2 - (2I_{Rb} + 1)^2}{2n_{Rb} \sigma_{SE}^{Rb-K} \bar{v}_{Rb-K}}. \quad (5)$$

For ³⁹K, ⁸⁵Rb and ¹³³Cs, $I_K = 1.5$, $I_{Rb} = 2.5$, $I_{Cs} = 3.5$, the relaxation rate for alkali-alkali spin-exchange collisions

$$R_{SE}^{RbRb} = \left(\frac{g\mu_B B}{Q(0)_{Rb} \hbar} \right)^2 \frac{Q(0)_{Rb}^2 - (2I_{Rb} + 1)^2}{2n_{Rb} \sigma_{SE}^{Rb-Rb} \bar{v}_{Rb-Rb}}, \quad (6)$$

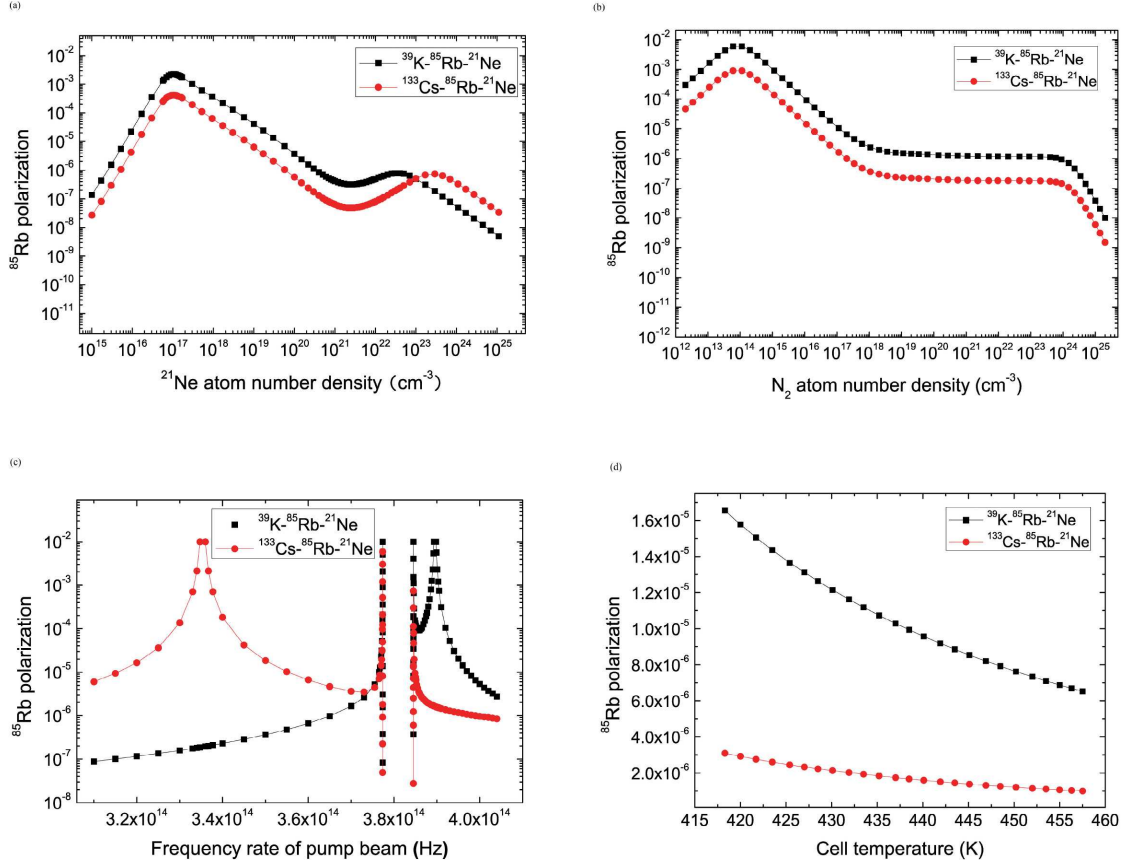
$$R_{SE}^{KRb} = \left(\frac{g\mu_B B}{Q(0)_K \hbar} \right)^2 \frac{Q(0)_K^2 - (2I_K + 1)^2}{2n_K \sigma_{SE}^{K-Rb} \bar{v}_{K-Rb}}, \quad (7)$$

$$R_{SE}^{RbK} = \left(\frac{g\mu_B B}{Q(0)_{Rb} \hbar} \right)^2 \frac{Q(0)_{Rb}^2 - (2I_{Rb} + 1)^2}{2n_{Rb} \sigma_{SE}^{Rb-K} \bar{v}_{Rb-K}}, \quad (8)$$

$$R_{SE}^{KK} = \left(\frac{g\mu_B B}{Q(0)_K \hbar} \right)^2 \frac{Q(0)_K^2 - (2I_K + 1)^2}{2n_K \sigma_{SE}^{K-K} \bar{v}_{K-K}}. \quad (9)$$

where B is the external magnetic field. With sufficiently high alkali metal number density (at higher temperature) and in sufficiently low magnetic field, $R_{SE}^{KK} \approx R_{SE}^{RbRb} \approx R_{SE}^{RbK} \approx R_{SE}^{KRb} \approx 0$. In the absence of spin-exchange relaxation, spin destruction collisions due to the spin-rotation interaction ⁴⁶, become a limiting factor. For low polarization limit, we take $Q(P_K^e) \approx Q(0)_K$, $Q(P_{Rb}^e) \approx Q(0)_{Rb}$, σ_{SE}^{K-Rb} is the spin-exchange cross section of ³⁹K and ⁸⁵Rb by spin-exchange collisions with each other, the value of relevant parameters are given at TABLE 1.

We choose one of ^{21}Ne number density n_{Ne} , N_2 number density n_{N_2} , cell temperature T , frequency rate of pump beam ν , photon number flux $\Phi_{D1}^K(\Phi_{D1}^{Cs})$, mole fraction of ^{85}Rb , cell effective radius a , pump beam spot radius a_p and power density of pump beam $I_{PI}^K(I_{PI}^{Cs})$, the input rotation velocity in the x direction Ω_x and y direction Ω_y , external magnetic field in the y direction B_y and z direction B_z by equation (4) as a variable (other parameters are invariable) to obtain the results that the polarization of the ^{39}K (^{133}Cs)- ^{85}Rb - ^{21}Ne HOPSERF magnetometer respectively change with the variable. Depending on suggestions and the typical conditions of the experiment group ^{34,35,54}, in order to facilitate the theoretical analysis, we take the mole fraction of ^{85}Rb atom $f_{Rb} = 0.97$, $n_{Ne} = 6 \times 10^{19} \text{ cm}^{-3}$, $\Phi_{D1}^K = \Phi_{D1}^{Cs} = 10^{20} / \text{s}$, $n_{N_2} = 2 \times 10^{17} \text{ cm}^{-3}$, $I_{PI}^K = I_{PI}^{Cs} = 0.02 \text{ W/cm}^2$, $\Omega_x = 7.292 \times 10^{-6} \text{ rad/s}$, $\Omega_y = 7.292 \times 10^{-5} \text{ rad/s}$, $B_y = 1 \times 10^{-12} \text{ T}$, $B_z = 2.1 \times 10^{-9} \text{ T}$, $a = 1 \text{ cm}$, $a_p = 1 \text{ cm}$, $\nu_p^K = \nu_p^{Cs} = 3.99 \times 10^{14} \text{ Hz}$ and $T = 457.5 \text{ K}$, at the moment, ^{39}K , ^{85}Rb and ^{133}Cs are in the SERF regime.



The ^{85}Rb polarization of ^{39}K (^{133}Cs)- ^{85}Rb - ^{21}Ne co-magnetometers change with the number density of the buffer gas ^{21}Ne in Fig. 2(a), the number density of the quench gas N_2 in Fig. 2(b), the frequency rate of pump beam in Fig. 2(c) and the cell temperature in Fig. 2(d), respectively. There is an anomalous behavior for the ^{85}Rb polarization changing with the frequency rate (when the frequency rate is around 3.8×10^{14} Hz).

To ensure the validity of the low polarization limit, we make the ^{85}Rb polarization be smaller than 0.01 and bigger than 0. The variations of the pumping rate of pump beam, the frequency shift, the B^n , the B^e , the alkali-alkali spin-exchange collisions relaxation rate related with ^{85}Rb

atom are shown in Fig.8 ~ Fig.13, respectively. Fig. 2 demonstrates the ^{85}Rb polarization of ^{39}K (^{133}Cs)- ^{85}Rb - ^{21}Ne co-magnetometers changes with n_{Ne} , n_{N2} , ν_p and T respectively.

Fig. 2(a) shows that ^{85}Rb polarization increases with the increasing n_{Ne} when n_{Ne} is smaller than a critical value about $1.0404 \times 10^{17} \text{ cm}^{-3}$ or bigger than about $2.5306 \times 10^{21} \text{ cm}^{-3}$ and smaller than about $3.4786 \times 10^{22} \text{ cm}^{-3}$ in ^{39}K - ^{85}Rb - ^{21}Ne and smaller than a critical value about $1.0328 \times 10^{17} \text{ cm}^{-3}$ or bigger than about $2.4929 \times 10^{21} \text{ cm}^{-3}$ and smaller than about $2.5809 \times 10^{23} \text{ cm}^{-3}$ in ^{133}Cs - ^{85}Rb - ^{21}Ne co-magnetometers, otherwise, ^{85}Rb polarization decreases. The ^{85}Rb polarization of ^{133}Cs - ^{85}Rb - ^{21}Ne co-magnetometer is smaller than the one of ^{39}K - ^{85}Rb - ^{21}Ne co-magnetometer when ^{21}Ne number density is smaller than about $9.8826 \times 10^{22} \text{ cm}^{-3}$.

From the formula of R_{SD}^{Rb} and Fig. 1(a), Fig. 8(a), Fig. 9(d), Fig. 10(a), Fig. 11(a), we can find that R_{SD}^{Rb} increases with the increasing n_{Ne} , $R_{wall-K-Rb-Ne}^{Rb-Ne}$, $R_{wall-K-Rb-Ne}^{Rb-Ne-N2}$, $R_{wall-Cs-Rb-Ne}^{Rb-Ne}$, $R_{wall-Cs-Rb-Ne}^{Rb-Ne-N2}$ decrease when ^{21}Ne atom number density n_{Ne} increases in Fig. 1(a), the R_p^K and R_p^{Cs} increase with increasing n_{Ne} when n_{Ne} is smaller than a critical value about $3.8892 \times 10^{22} \text{ cm}^{-3}$ and $2.6214 \times 10^{23} \text{ cm}^{-3}$, respectively (otherwise, R_p^K and R_p^{Cs} decrease with increasing n_{Ne}) in Fig. 8(a), $L_{K-Rb-Ne}^K$ and $L_{K-Rb-Ne}^{K-Rb}$, $L_{Cs-Rb-Ne}^{Cs}$ and $L_{Cs-Rb-Ne}^{Cs-Rb}$ decrease slowly with increasing n_{Ne} when the n_{Ne} is smaller than about $6 \times 10^{21} \text{ cm}^{-3}$ and $5.6 \times 10^{22} \text{ cm}^{-3}$ respectively (otherwise, they decrease rapidly) in Fig. 9(d), B^n increases rapidly when n_{Ne} is smaller than about $4.0 \times 10^{22} \text{ cm}^{-3}$ (then increases slowly and tends to a constant from the equation of B^n and T_{1n}) in Fig. 10(a), B^e increases with the increasing n_{Ne} when n_{Ne} is smaller than about $5.6071 \times 10^{21} \text{ cm}^{-3}$ in ^{39}K - ^{85}Rb - ^{21}Ne and $2.01 \times 10^{22} \text{ cm}^{-3}$ in ^{133}Cs - ^{85}Rb - ^{21}Ne co-magnetometer

respectively (then decreases) in Fig. 11(a). There is a biggest value for ^{85}Rb polarization when n_{Ne} is about $1.0404 \times 10^{17} \text{ cm}^{-3}$ in $^{39}\text{K}-^{85}\text{Rb}-^{21}\text{Ne}$ and $1.0328 \times 10^{17} \text{ cm}^{-3}$ in $^{133}\text{Cs}-^{85}\text{Rb}-^{21}\text{Ne}$ co-magnetometer, which is mainly determined by the R_{SD}^{Rb} and R_{wall}^{Rb} . When n_{Ne} is about $2.5809 \times 10^{23} \text{ cm}^{-3}$ in $^{39}\text{K}-^{85}\text{Rb}-^{21}\text{Ne}$ and $2.5809 \times 10^{23} \text{ cm}^{-3}$ in $^{133}\text{Cs}-^{85}\text{Rb}-^{21}\text{Ne}$ co-magnetometer, there is also a biggest value for ^{85}Rb polarization, which is mainly determined by the R_{SD}^{Rb} , R_{wall}^{Rb} and R_p^K (R_p^{Cs}).

Fig. 2(b) demonstrates that ^{85}Rb polarization increases with increasing n_{N_2} when n_{N_2} is smaller than about $8.2655 \times 10^{13} \text{ cm}^{-3}$ in $^{39}\text{K}-^{85}\text{Rb}-^{21}\text{Ne}$ and $^{133}\text{Cs}-^{85}\text{Rb}-^{21}\text{Ne}$ co-magnetometers, otherwise, the ^{85}Rb polarization decreases. When n_{N_2} is in the range about $1 \times 10^{18} \text{ cm}^{-3} \sim 1 \times 10^{24} \text{ cm}^{-3}$, the ^{85}Rb polarization decreases slowly with the increasing n_{N_2} . From the formula of R_{SD}^{Rb} and Fig. 1(b), Fig. 11(b), we can find that R_{SD}^{Rb} increases with the increasing n_{N_2} , $R_{wall-K-Rb-Ne}^{Rb-N_2}$, $R_{wall-K-Rb-Ne}^{Rb-Ne-N_2}$, $R_{wall-Cs-Rb-Ne}^{Rb-N_2}$ and $R_{wall-Cs-Rb-Ne}^{Rb-Ne-N_2}$ decrease when n_{N_2} increases, $R_{wall-K-Rb-Ne}^{Rb-Ne}$ and $R_{wall-Cs-Rb-Ne}^{Rb-Ne}$ don't change when n_{N_2} increases in Fig. 1(b), B^e decreases slowly when n_{N_2} is smaller than about $4.0 \times 10^{19} \text{ cm}^{-3}$ in $^{39}\text{K}-^{85}\text{Rb}-^{21}\text{Ne}$ and $^{133}\text{Cs}-^{85}\text{Rb}-^{21}\text{Ne}$ co-magnetometer respectively, then begin to decrease rapidly in Fig. 11(b). There is a biggest value for ^{85}Rb polarization when n_{N_2} is about $8.2655 \times 10^{13} \text{ cm}^{-3}$ in $^{39}\text{K}-^{85}\text{Rb}-^{21}\text{Ne}$ and $^{133}\text{Cs}-^{85}\text{Rb}-^{21}\text{Ne}$ co-magnetometers, which is mainly determined by the R_{SD}^{Rb} and R_{wall}^{Rb} .

Fig. 2(c) shows that ^{85}Rb polarization of $^{39}\text{K}-^{85}\text{Rb}-^{21}\text{Ne}$ co-magnetometer increases when the ν_p increases but is smaller than a critical value about $3.7735 \times 10^{14} \text{ Hz}$ or in the range about $3.7736 \times 10^{14} \text{ Hz} \sim 3.8452 \times 10^{14} \text{ Hz}$, or bigger than $3.8577 \times 10^{14} \text{ Hz}$, decreases when the ν_p is in the range about $3.7735 \times 10^{14} \text{ Hz} \sim 3.7736 \times 10^{14} \text{ Hz}$, or $3.8453 \times 10^{14} \text{ Hz} \sim 3.8577 \times 10^{14} \text{ Hz}$, or

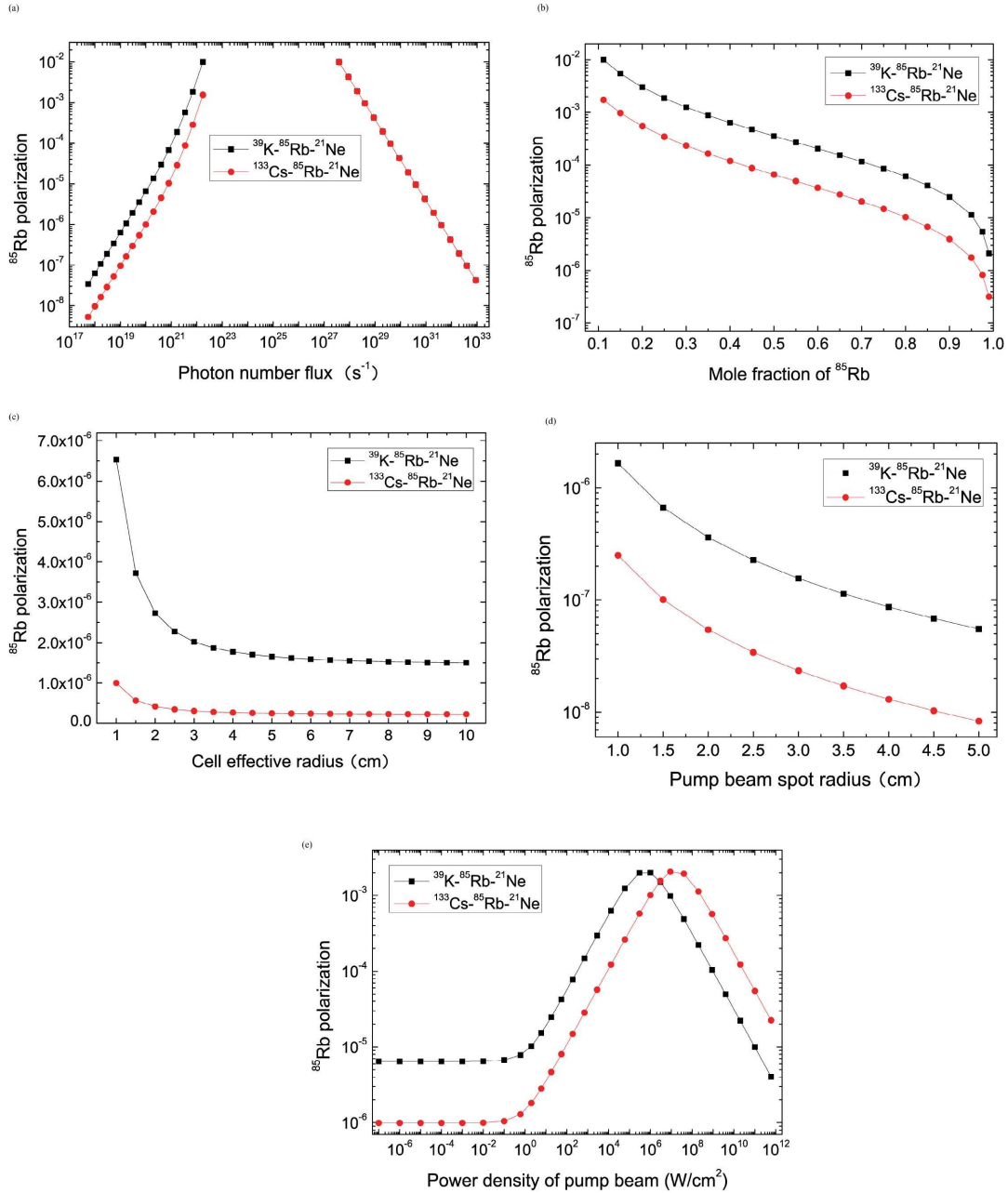
$3.8981 \times 10^{14} \text{ Hz} \sim 4.04 \times 10^{14} \text{ Hz}$. The ^{85}Rb polarization of ^{133}Cs - ^{85}Rb - ^{21}Ne co-magnetometer increases when the ν_p increases but is smaller than a critical value about $3.3475 \times 10^{14} \text{ Hz}$ or in the range about $3.724 \times 10^{14} \text{ Hz} \sim 3.7735 \times 10^{14} \text{ Hz}$, or $3.8452 \times 10^{14} \text{ Hz} \sim 3.8453 \times 10^{14} \text{ Hz}$. When the ν_p is in the range $3.3597 \times 10^{14} \text{ Hz} \sim 3.724 \times 10^{14} \text{ Hz}$, $3.7735 \times 10^{14} \text{ Hz} \sim 3.7736 \times 10^{14} \text{ Hz}$, or bigger than about $3.8453 \times 10^{14} \text{ Hz}$, the ^{85}Rb polarization decreases with increasing ν_p .

From the formula of the ^{85}Rb polarization and Fig. 8(e), Fig. 9(b), Fig. 11(c), we can find that R_p^K and R_p^{Cs} increase with increasing ν_p when the ν_p is smaller than a critical value about $3.8956 \times 10^{14} \text{ Hz}$ and $3.3535 \times 10^{14} \text{ Hz}$, respectively, otherwise, R_p^K and R_p^{Cs} decrease with the increasing ν_p in Fig. 8(e). The illustrations in Fig. 9(b) demonstrate that $L_{K-Rb-Ne}^K$ decreases with increasing ν_p when the ν_p is smaller than about $3.8954 \times 10^{14} \text{ Hz}$ and bigger than about $3.8957 \times 10^{14} \text{ Hz}$, otherwise, $L_{K-Rb-Ne}^K$ increases. $L_{Cs-Rb-Ne}^{Cs}$ decreases with the increasing ν_p when the ν_p is smaller than about $3.3533 \times 10^{14} \text{ Hz}$ and bigger than about $3.3536 \times 10^{14} \text{ Hz}$, otherwise, $L_{Cs-Rb-Ne}^{Cs}$ increases. $L_{K-Rb-Ne}^{Rb}$ increases with increasing ν_p when the ν_p is smaller than about $3.7735 \times 10^{14} \text{ Hz}$. When the ν_p is in the range about $3.7736 \times 10^{14} \text{ Hz} \sim 3.8093 \times 10^{14} \text{ Hz}$, $L_{K-Rb-Ne}^{Rb}$ and $L_{K-Rb-Ne}^{K-Rb}$ are negative and increase. When the ν_p is in the range $3.8094 \times 10^{14} \text{ Hz} \sim 3.8451 \times 10^{14} \text{ Hz}$, $L_{K-Rb-Ne}^{Rb}$ and $L_{K-Rb-Ne}^{K-Rb}$ are negative and decrease. When the ν_p is bigger than about $3.8452 \times 10^{14} \text{ Hz}$, $L_{K-Rb-Ne}^{Rb}$ is positive and decreases. $L_{K-Rb-Ne}^{K-Rb}$ is negative and decreases when the frequency rate is smaller than about $3.5429 \times 10^{14} \text{ Hz}$. When the ν_p is in the range $3.5429 \times 10^{14} \text{ Hz} \sim 3.7735 \times 10^{14} \text{ Hz}$, $L_{K-Rb-Ne}^{K-Rb}$ increases with increasing ν_p . When the ν_p is in the range about $3.8452 \times 10^{14} \text{ Hz} \sim 3.8954 \times 10^{14} \text{ Hz}$, $L_{K-Rb-Ne}^{K-Rb}$ decreases. When the ν_p is in the range about $3.8955 \times 10^{14} \text{ Hz} \sim 3.8957 \times 10^{14} \text{ Hz}$, $L_{K-Rb-Ne}^{K-Rb}$ increases. When the ν_p is bigger than

about 3.8957×10^{14} Hz, $L_{K-Rb-Ne}^{K-Rb}$ decreases. $L_{Cs-Rb-Ne}^{Cs-Rb}$ decreases with increasing ν_p when the ν_p is in the range about 3.1×10^{14} Hz \sim 3.3533×10^{14} Hz and 3.3536×10^{14} Hz \sim 3.6017×10^{14} Hz, 3.8094×10^{14} Hz \sim 3.8451×10^{14} Hz, 3.8452×10^{14} Hz \sim 4.04×10^{14} Hz. $L_{Cs-Rb-Ne}^{Cs-Rb}$ increases when the ν_p is in the range about 3.3534×10^{14} Hz \sim 3.3536×10^{14} Hz, 3.6017×10^{14} Hz \sim 3.7735×10^{14} Hz and 3.7736×10^{14} Hz \sim 3.8093×10^{14} Hz. B^e increases with increasing ν_p when the ν_p is smaller than about 3.8955×10^{14} Hz in ^{39}K - ^{85}Rb - ^{21}Ne and 3.3534×10^{14} Hz in ^{133}Cs - ^{85}Rb - ^{21}Ne co-magnetometer respectively, then decreases in Fig. 11(c), which is caused by the pumping rate due to the pumping rate has the same pattern of change from Fig. 8(e). Therefore, the change of ^{85}Rb polarization with the ν_p is mainly determined by the pumping rate of the pump beam, the frequency shift and B^e . The anomalous behavior of the change of ^{85}Rb polarization with the ν_p when the ν_p is around 3.8×10^{14} Hz, which is different from Fig. 8(e) and Fig. 11(c), is mainly determined by the frequency shift.

Fig. 2(d) demonstrates that ^{85}Rb polarization decreases with the increasing T . The ^{85}Rb polarization of ^{133}Cs - ^{85}Rb - ^{21}Ne co-magnetometer is smaller than the one of ^{39}K - ^{85}Rb - ^{21}Ne co-magnetometer. From the formula of the R_{SD}^{Rb} and Fig. 1(c), Fig. 8(f), Fig. 9(e), Fig. 10(b), Fig. 12(d), Fig. 13(b), we can find that R_{SD}^{Rb} increases with increasing T . $R_{wall-K-Rb-Ne}^{Rb-N2}$, $R_{wall-K-Rb-Ne}^{Rb-Ne-N2}$, $R_{wall-Cs-Rb-Ne}^{Rb-N2}$, $R_{wall-Cs-Rb-Ne}^{Rb-Ne-N2}$, $R_{wall-K-Rb-Ne}^{Rb-Ne}$ and $R_{wall-Cs-Rb-Ne}^{Rb-Ne}$ increase with increasing T in Fig. 1(c) for the increasing T makes the number density and relative velocity of ^{85}Rb atoms bigger and more ^{85}Rb atoms move towards the wall. Fig. 8(f) shows that R_p^K and R_p^{Cs} increase with increasing T , duo to the increasing T increases the linewidth of the K-Ne and Cs-Ne pressure broadening, which make R_p^K and R_p^{Cs} increase. Fig. 9(e) shows that

$L_{K-Rb-Ne}^K$, $L_{Cs-Rb-Ne}^{Cs}$, $L_{K-Rb-Ne}^{K-Rb}$ and $L_{Cs-Rb-Ne}^{Cs-Rb}$ decreases slowly with increasing T , duo to the increasing T increases the linewidth of the K-Ne and Cs-Ne pressure broadening, which make $L_{K-Rb-Ne}^K$, $L_{Cs-Rb-Ne}^{Cs}$, $L_{K-Rb-Ne}^{K-Rb}$ and $L_{Cs-Rb-Ne}^{Cs-Rb}$ decrease. However, $L_{K-Rb-Ne}^{Rb}$ and $L_{Cs-Rb-Ne}^{Rb}$ don't change with the T for $L_{K-Rb-Ne}^{Rb}$ and $L_{Cs-Rb-Ne}^{Rb}$ have nothing to do with the T . Fig. 10(b) shows that B^n increases with increasing T and B^n tends to a constant in the end duo to only R_{Rb-Ne}^{se} changes with the T from the equation of B^n and R_{Rb-Ne}^{se} increases with the increasing T . B^e increases with increasing T in Fig. 12(d). R_{KRbNe}^{RbK} , R_{CsRbNe}^{RbCs} , R_{KRbNe}^{RbRb} , R_{CsRbNe}^{RbRb} , R_{KRbNe}^{EE} , R_{CsRbNe}^{EE} decrease with the increasing T in Fig. 13(b) for the increasing T making R_{Rb-K}^{SE} , R_{Rb-Rb}^{SE} and R_{Rb-Cs}^{SE} increase, which is inversely proportional to the R_{KRbNe}^{RbK} , R_{KRbNe}^{RbRb} , R_{CsRbNe}^{RbRb} , R_{CsRbNe}^{RbCs} in equation (5), respectively. Therefore, the total effect of the R_{SD}^{Rb} , the pumping rate of the pump beam (R_p^K and R_p^{Cs}), the frequency shift ($L_{K-Rb-Ne}^K$, $L_{Cs-Rb-Ne}^{Cs}$, $L_{K-Rb-Ne}^{K-Rb}$ and $L_{Cs-Rb-Ne}^{Cs-Rb}$), B^n , B^e and the alkali-alkali spin-exchange collisions relaxation rate (R_{KRbNe}^{RbK} , R_{CsRbNe}^{RbCs} , R_{KRbNe}^{RbRb} , R_{CsRbNe}^{RbRb} , R_{KRbNe}^{EE} , R_{CsRbNe}^{EE}) make the ^{85}Rb polarization decrease with the increasing T .



The ^{85}Rb polarization of ^{39}K (^{133}Cs)- ^{85}Rb - ^{21}Ne co-magnetometers change with the photon number flux in Fig. 3(a), the mole fraction of ^{85}Rb in Fig. 3(b), the cell effective radius in Fig. 3(c), the pump beam spot radius in Fig. 3(d) when $a = 5\text{cm}$ and the power density of pump

beam in Fig. 3(e).

Fig. 3 shows that the ^{85}Rb polarization of ^{39}K (^{133}Cs)- ^{85}Rb - ^{21}Ne co-magnetometers changes with the photon number flux Φ_{D1} , mole fraction of ^{85}Rb f_{Rb} , cell effective radius a , pump beam spot radius a_p and power density of pump beam I_{PI} . Fig. 3(a) demonstrates that ^{85}Rb polarization in ^{39}K - ^{85}Rb - ^{21}Ne co-magnetometer increases with increasing Φ_{D1} when the Φ_{D1} is smaller than about 1.7315×10^{22} /s and decreases when the Φ_{D1} is bigger than 3.8416×10^{27} /s. ^{85}Rb polarization in ^{133}Cs - ^{85}Rb - ^{21}Ne co-magnetometer increases with increasing Φ_{D1} when the Φ_{D1} is smaller than about 4.3672×10^{22} /s and decreases when Φ_{D1} is bigger than about 3.8203×10^{27} /s. From the formula of the ^{85}Rb polarization and Fig. 8(d), Fig. 9(a), Fig. 12(a), we can find that R_p^K (R_p^{Cs}), the frequency shift and B^e increase with the increasing Φ_{D1} . B^e increases rapidly with the increasing Φ_{D1} when the Φ_{D1} is smaller than about $5 \times 10^{24} \text{ s}^{-1}$ in ^{39}K - ^{85}Rb - ^{21}Ne and $3 \times 10^{25} \text{ s}^{-1}$ in ^{133}Cs - ^{85}Rb - ^{21}Ne co-magnetometer respectively, then increases slowly and tends to a constant in Fig. 12(a) due to only the pumping rate increases with the increasing Φ_{D1} in the equation of B^e and P_{zRb}^e , P_{zRb}^e has the same pattern of change, which makes the B^e have the change rule above. Therefore, the increase process of the ^{85}Rb polarization is determined by R_p^K (R_p^{Cs}), the frequency shift and B^e , the decrease process of the ^{85}Rb polarization is mainly determined by R_p^K (R_p^{Cs}) and the frequency shift for B^e tending to a constant.

Fig. 3(b) shows that ^{85}Rb polarizations decrease with increasing mole fraction of ^{85}Rb f_{Rb} . From the formula of the D_r , R_{SD}^{Rb} and Fig. 11(d), Fig. 13(a), we can find that D_r decreases and R_{SD}^{Rb} increases with the increasing f_{Rb} . When the f_{Rb} is smaller than about 0.0318 in ^{39}K - ^{85}Rb - ^{21}Ne and

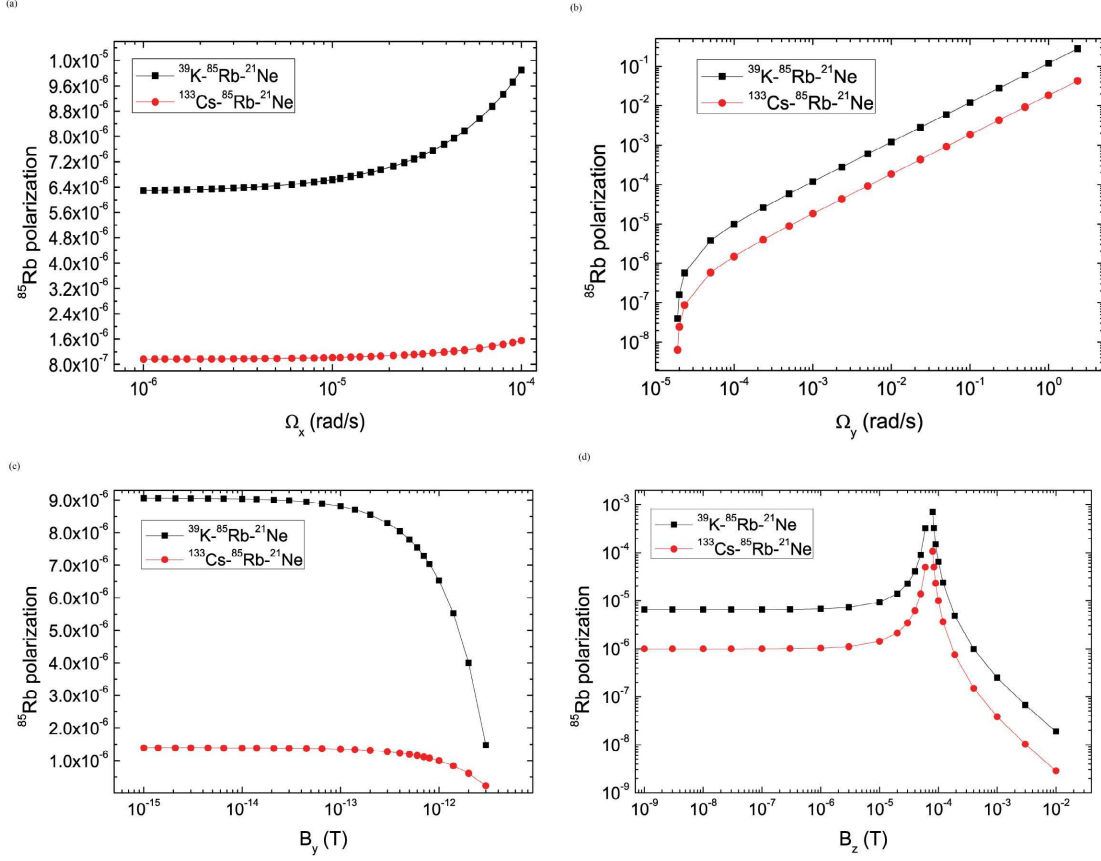
0.0135 in ^{133}Cs - ^{85}Rb - ^{21}Ne co-magnetometer respectively, B^e increases with the increasing f_{Rb} , otherwise, B^e decreases in Fig. 11(d). Fig. 13(a) shows that the R_{KRbNe}^{RbK} , R_{CsRbNe}^{RbCs} , R_{KRbNe}^{RbRb} , R_{CsRbNe}^{RbRb} , R_{KRbNe}^{EE} , R_{CsRbNe}^{EE} decrease with the increasing f_{Rb} . Therefore, the decrease process of the ^{85}Rb polarization is determined by D_r , R_{SD}^{Rb} , B^e and R_{KRbNe}^{RbK} , R_{CsRbNe}^{RbCs} , R_{KRbNe}^{RbRb} , R_{CsRbNe}^{RbRb} , R_{KRbNe}^{EE} , R_{CsRbNe}^{EE} , where the D_r and R_{SD}^{Rb} play important roles.

Fig. 3(c) demonstrates that ^{85}Rb polarizations decrease with increasing cell effective radius a . From the formula of the ^{85}Rb polarization and Fig. 1(d), Fig. 12(b), we can find that the wall relaxation rate $R_{wall-K-Rb-Ne}^{Rb-Ne}$, $R_{wall-K-Rb-Ne}^{Rb-N2}$, $R_{wall-K-Rb-Ne}^{Rb-Ne-N2}$, $R_{wall-Cs-Rb-Ne}^{Rb-Ne}$, $R_{wall-Cs-Rb-Ne}^{Rb-N2}$ and $R_{wall-Cs-Rb-Ne}^{Rb-Ne-N2}$ decreases when the a increases in Fig. 1(d) and B^e increases when a increases in Fig. 12(b), therefore, the decrease process of the ^{85}Rb polarization is determined by the wall relaxation rate and B^e , where the wall relaxation rate plays a decisive role.

Fig. 3(d) demonstrates that ^{85}Rb polarizations decrease with increasing pump beam spot radius a_p when $a = 5\text{cm}$. From the formula of the ^{85}Rb polarization and Fig. 8(b), Fig. 9(f), Fig. 12(c), we can find that R_p^K , R_p^{Cs} , the frequency shift and B^e decreases with the increasing a_p due to the increasing a_p increases the transverse area of the pumping light A_t , which makes R_p^K , R_p^{Cs} and the frequency shift decrease. The B^e decreases with the increasing a_p due to the increasing a_p makes the R_p^K (R_p^{Cs}) decrease, which decreases the P_{zRb}^e and the decreasing P_{zRb}^e makes the B^e decrease.

Fig. 3(e) shows that ^{85}Rb polarization increases when the power density of pump beam I_{PI}^K and I_{PI}^{Cs} increase, but is smaller than a critical value about $5.499 \times 10^5 \text{ W/cm}^2$ and 1.6156×10^7

W/cm^2 , respectively, otherwise, it will decrease. When the I_{PI}^K is in the range about $1 \text{ W}/\text{cm}^2 \sim 5.499 \times 10^5 \text{ W}/\text{cm}^2$ and I_{PI}^{Cs} is in the range about $0.2 \text{ W}/\text{cm}^2 \sim 1.6156 \times 10^7 \text{ W}/\text{cm}^2$, the ^{85}Rb polarization increases rapidly. From the formula of the Γ_{D1}^K and Γ_{D1}^{Cs} , Fig. 8(c), Fig. 9(c), Fig. 12(e), we can find that Γ_{D1}^K and Γ_{D1}^{Cs} increase with the increasing I_{PI}^K and I_{PI}^{Cs} , respectively. R_p^K and R_p^{Cs} increase with increasing I_{PI}^K and I_{PI}^{Cs} when I_{PI}^K is smaller than a critical value about $5.499 \times 10^5 \text{ W}/\text{cm}^2$ and I_{PI}^{Cs} is smaller than a critical value about $1.6156 \times 10^7 \text{ W}/\text{cm}^2$, respectively, otherwise, R_p^K and R_p^{Cs} decrease with the increasing power density. Fig. 9(c) shows that $L_{K-Rb-Ne}^K$ and $L_{Cs-Rb-Ne}^{Cs}$ decrease slowly with the increasing I_{PI}^K and I_{PI}^{Cs} when the I_{PI}^K and I_{PI}^{Cs} is smaller than about $10^5 \text{ W}/\text{cm}^2$ and $10^6 \text{ W}/\text{cm}^2$, respectively, otherwise, $L_{K-Rb-Ne}^K$ and $L_{Cs-Rb-Ne}^{Cs}$ decrease rapidly. $L_{K-Rb-Ne}^{Rb}$ and $L_{Cs-Rb-Ne}^{Rb}$ don't change with the I_{PI}^K and I_{PI}^{Cs} for $L_{K-Rb-Ne}^{Rb}$ and $L_{Cs-Rb-Ne}^{Rb}$ have nothing to do with the power density. $L_{K-Rb-Ne}^{K-Rb}$ and $L_{Cs-Rb-Ne}^{Cs-Rb}$ decrease with the increasing I_{PI}^K and I_{PI}^{Cs} . B^e increases when the I_{PI}^K and I_{PI}^{Cs} increase, but is smaller than a critical value about $5.499 \times 10^5 \text{ W}/\text{cm}^2$ and $1.6156 \times 10^7 \text{ W}/\text{cm}^2$ in Fig. 12(e), respectively, otherwise, it will decrease. Therefore, the change process of the ^{85}Rb polarization is determined by the pumping rate of the pump beam, the frequency shift and B^e , where the the pump beam and B^e play a decisive role. When the I_{PI}^K and I_{PI}^{Cs} are smaller than about $2.883 \times 10^6 \text{ W}/\text{cm}^2$, the ^{85}Rb polarization in the ^{39}K - ^{85}Rb - ^{21}Ne co-magnetometer is even bigger than the one in the ^{133}Cs - ^{85}Rb - ^{21}Ne co-magnetometer.



The ^{85}Rb polarization of ^{39}K (^{133}Cs)- ^{85}Rb - ^{21}Ne co-magnetometers change with the input rotation velocity in the x direction in Fig. 4(a) and y direction in Fig. 4(b), the external magnetic field in the y direction B_y in Fig. 4(c) and z direction B_z in Fig. 4(d), respectively.

Fig. 4 shows that the ^{85}Rb polarization of ^{39}K (^{133}Cs)- ^{85}Rb - ^{21}Ne co-magnetometers change with the input rotation velocity in the x direction and y direction. Fig. 4(a) demonstrates that the ^{85}Rb polarizations increase with increasing input rotation velocity in the x direction Ω_x . Fig. 4(b) shows that the ^{85}Rb polarizations increase with increasing Ω_y . When L_z is some negative value,

$$\frac{\Omega_y}{\gamma^n} + \frac{L_z}{R_{tot}^{Rb}/\gamma^e} \frac{\Omega_x}{\gamma^n} = 0, \text{ which can help eliminate the effect of the input rotation velocity } \Omega_x \text{ and } \Omega_y \text{ on}$$

the ^{85}Rb polarization. Fig. 4(c) demonstrates that ^{85}Rb polarizations decrease with increasing external magnetic field in the y direction B_y . Fig. 4(d) shows that ^{85}Rb polarizations increase slowly with increasing external magnetic field in the z direction B_z when B_z is smaller than about 10^{-5} T and increase rapidly when B_z is bigger than about 10^{-5} T but smaller than about 6.9588×10^{-5} T (^{85}Rb polarization is about 0.01) in ^{39}K - ^{85}Rb - ^{21}Ne and 7.0895×10^{-5} W/cm² (^{85}Rb polarization is about 0.01) in ^{133}Cs - ^{85}Rb - ^{21}Ne co-magnetometer. When B_z is bigger than about 7.3907×10^{-5} T (^{85}Rb polarization is about 0.01) in ^{39}K - ^{85}Rb - ^{21}Ne and 7.2585×10^{-5} W/cm² (^{85}Rb polarization is about 0.01) in ^{133}Cs - ^{85}Rb - ^{21}Ne co-magnetometer, the ^{85}Rb polarization decreases rapidly. The change of B_z will make the compensation magnetic field δB_z change, which will affect the ^{85}Rb polarization.

The fundamental sensitivity of the hybrid optical pumping SERF co-magnetometer. To improve the practicability of the hybrid optical pumping SERF co-magnetometers, it is necessary for us to investigate the fundamental sensitivity of the co-magnetometers to improve the sensitivity, stability of the co-magnetometers and realize the miniaturization of the co-magnetometers. The fundamental, shot-noise-limited sensitivity of an atomic gyroscope based on the co-magnetometer is given by ^{17,59}

$$\delta\Omega = \frac{\gamma^n}{\gamma^e} \frac{1}{\sqrt{nT_2Vt}}, \quad (10)$$

where γ^n is the nuclear gyromagnetic ratio of the noble gas atom, γ^e is the electron gyromagnetic ratio of the alkali metal atom, γ^e ($\gamma^e = \frac{g\mu_B}{\hbar}$) ^{27,59}, g is the electron g -factor, μ_B is the Bohr magneton, n is the density of alkali metal atoms, V is the measurement volume, t is the measurement time, T_2 is the transverse spin relaxation time, $\frac{1}{T_2} = R_{SD} + R_{wall} + Q(P^e)R_{SE}^e$. For the transverse

spin relaxation time of the co-magnetometers, we need consider the spin destruction relaxation R_{SD} caused by Ne, N₂, alkali metal atom A and B, the relaxation rates due to diffusion of alkali metal atoms A and B to the wall ¹⁷ R_{wall}^A and R_{wall}^B , the relaxation rate due to alkali-alkali spin-exchange collisions ⁶⁰ R_{SE}^{ee} , $R_{SE}^{ee} = R_{SE}^{AA} + R_{SE}^{AB} + R_{SE}^{BA} + R_{SE}^{BB}$, which cannot be ignored for large external magnetic field B and is negligible in SERF regime (when T is higher than 418.3 K, B is smaller than 10^{-10} T, $R_{SE}^{ee} \approx 0$), the pumping rate of pump beam R_p and the pumping rate of atom B R_B (R_B is a function of R_p), hence, $\frac{1}{T_2} = R_{SD}^A + R_{SD}^B + R_{wall}^A + R_{wall}^B + Q(P^e)R_{SE}^{ee} + R_p + R_B$, we substitute this term into equation (10) and obtain

$$\delta\Omega = \frac{\gamma^n \sqrt{R_{SD}^{AB} + R_{Wall} + Q(P^e)R_{SE}^{ee} + R_p + R_B}}{\gamma^e \sqrt{nVt}}. \quad (11)$$

where $R_{SD}^{AB} = R_{SD}^A + R_{SD}^B$, $R_{Wall} = R_{wall}^A + R_{wall}^B$. However, because alkali metal atom B is probed atom, only these items associated with atom B will be considered in the experiments, we don't consider those items irrelevant to atom B, for the low polarization limit, we acquire the fundamental sensitivity of the co-magnetometers due to the shot-noise as following

$$\delta\Omega' = \frac{\gamma^n \sqrt{R_{wall}^B + R_{SD} + R_B + Q(0)_B R_{SE}^{EE}}}{\gamma^e \sqrt{n_B V t}}. \quad (12)$$

where $R_{wall} = Q(0)_B D_{buffer}^B \left(\frac{\sqrt{1+T/273.15}}{P_{buffer}/1\text{amg}} \right) \left(\frac{\pi}{a} \right)^2 + Q(0)_B D_{quench}^B \left(\frac{\sqrt{1+T/273.15}}{P_{quench}/1\text{amg}} \right) \left(\frac{\pi}{a} \right)^2$, D are the diffusion coefficients of the alkali atom within Ne and N₂ respectively, $R_{wall}^B = R_{wall}^{B-Ne} + R_{wall}^{B-N_2}$. D_{buffer}^B is the diffusion constant of the alkali atom B within the buffer gas ³⁹⁻⁴¹ in units of cm²/s and is given at 1 amg and 273 K, D_{quench}^B is the diffusion constant of the alkali atom B within the quench gas ⁴⁰⁻⁴² in units of cm²/s and is given at 1 amg and 273 K, 1amg = 2.69×10^{19} cm⁻³, P_{buffer} is the pressure intensity of buffer gas in amg, P_{quench} is the pressure intensity of quench gas in amg, a is the equivalent radius of vapor cell, $R_{SD} = n_{Ne} \sigma_{SD}^{B-Ne} \bar{v}_{B-Ne} + n_{N_2} \sigma_{SD}^{B-N_2} \bar{v}_{B-N_2} +$

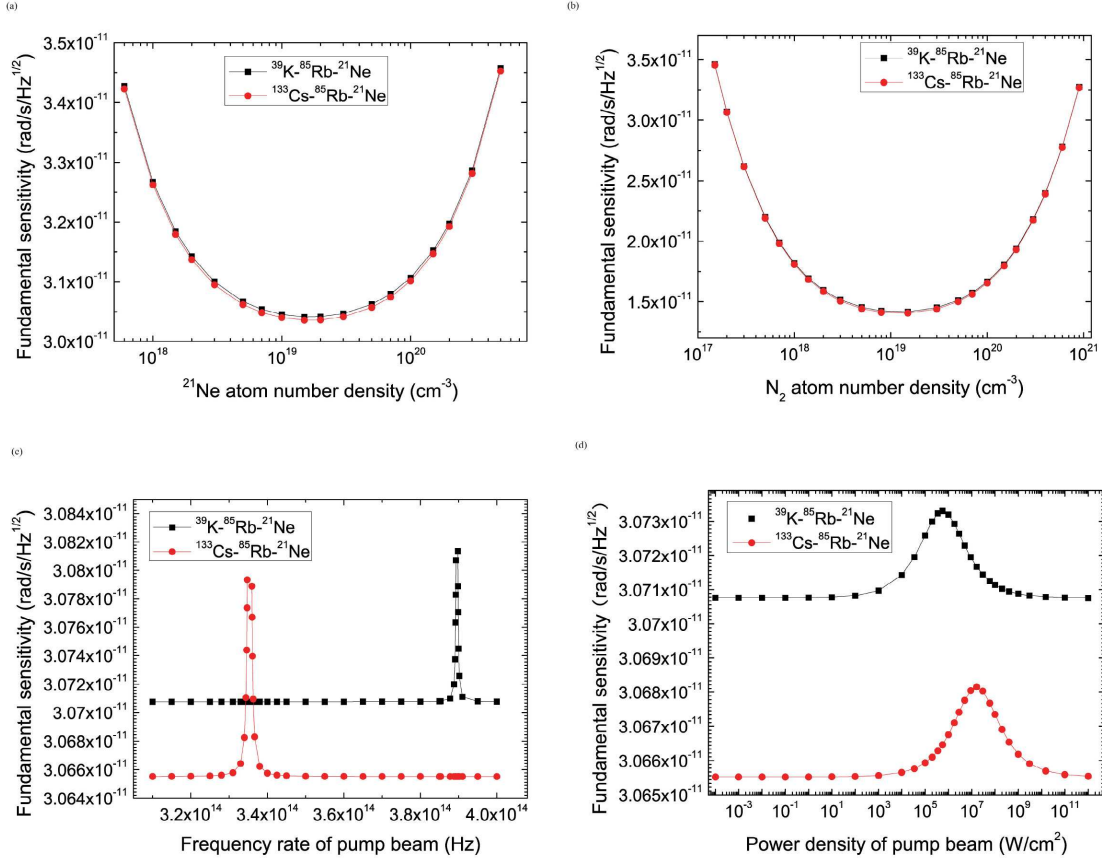
$$n_B \sigma_{SD}^{B-B} \bar{v}_{B-B} + n_B \sigma_{SD}^{B-A} \bar{v}_{B-A} + n_A \sigma_{SD}^{A-B} \bar{v}_{A-B}, R_B = D_r R_p, R_{SE}^{EE} = R_{SE}^{BB} + R_{SE}^{BA}, R_{SE}^{BB} = \left(\frac{g\mu_B B}{q(0)_B \hbar} \right)^2 \frac{q(0)_B^2 - (2I_B + 1)^2}{2k_{SE}^{B-B} n_B}, R_{SE}^{BA} = \left(\frac{g\mu_B B}{q(0)_B \hbar} \right)^2 \frac{q(0)_B^2 - (2I_B + 1)^2}{2k_{SE}^{B-A} n_B}.$$

In the limit of fast spin-exchange and small magnetic field, the spin-exchange relaxation rate vanishes for sufficiently small magnetic field³⁶. In equation (12), we can find that the fundamental sensitivity of the co-magnetometers increases when part or all of R_{wall}^B , R_{SD} , R_B , R_{SE}^{BB} , R_{SE}^{AB} and R_{SE}^{BA} (the later three terms are approximately zero in sufficiently low magnetic field and the co-magnetometer is in the SERF regime, which is helpful for us to study how B influence the SERF regime and fundamental sensitivity of the co-magnetometers) decrease, n_B , V and t increase. For the expressions of R_{wall}^B , R_{SD} , R_B , R_{SE}^{BB} , R_{SE}^{AB} , R_{SE}^{BA} , n_B , V and t , we just need to consider the fundamental sensitivity of the co-magnetometers change with one of the cell effective radius a , n_{Ne} , n_{N_2} , t , cell temperature T , pumping rate of pump beam (R_p^K and R_p^{Cs}), external magnetic field B and measurement volume V .

As we discussed in our previous work²⁴, diffusion of alkali metal atoms A and B to the wall will corrode the vapor cell and decrease the fundamental sensitivity of the co-magnetometers. Sufficiently many buffer gas will reduce diffusion of alkali metal atoms A and B to the wall. The probed alkali-metal atoms have a large absorption effect on the pumping beam, it's an additional relaxation item for the alkali-metal atoms of the co-magnetometers. The spin exchange rate between alkali metal atoms A and alkali metal atoms B plays a similar ‘‘pumping beam’’ action. Atom B is polarized by the spin exchange collision between alkali metal atoms A and B. The pumping effect of probe beam means circularly polarized light in the probe beam pumps alkali-metal atoms.

The outer electrons of the alkali metal atoms are polarized by the pumping beam, the polarized electrons undergo Larmor precession under the external magnetic field.

We take ^{39}K and ^{133}Cs atom as A atom, ^{85}Rb as B atom, one of the f_{Rb} , n_{Ne} , n_{N_2} , t , T , $\Phi_{D1}^K(\Phi_{D1}^{Cs})$, $\nu_p^K(\nu_p^{Cs})$, $I_{PI}^K(I_{PI}^{Cs})$, a , a_p , B (it is helpful for us to study how B influence the SERF regime and fundamental sensitivity of the co-magnetometers) and V in equation (12) as a variable (other parameters are invariable) to obtain the results that the fundamental sensitivity of the co-magnetometers based on ^{39}K - ^{85}Rb - ^{21}Ne and ^{133}Cs - ^{85}Rb - ^{21}Ne change with the variable. Depending on suggestions and the typical conditions of the experiment group ^{34,35,54}, in order to facilitate the theoretical analysis, we take $f_{Rb} = 0.97$, $n_{Ne} = 6 \times 10^{19} \text{ cm}^{-3}$, $n_{N_2} = 2 \times 10^{17} \text{ cm}^{-3}$, $\Phi_{D1}^K = \Phi_{D1}^{Cs} = 10^{20} \text{ /s}$, $I_{PI}^K = I_{PI}^{Cs} = 0.02W/cm^2$, $a = 1 \text{ cm}$, $a_p = 1 \text{ cm}$, $\nu_p^K = \nu_p^{Cs} = 3.99 \times 10^{14} \text{ Hz}$, $T = 457.5 \text{ K}$, $V = 1 \text{ cm}^3$, $t = 100 \text{ s}$ and $B = 10^{-15} \text{ T}$ ($R_{SE}^{ee} \approx 0$). The variations of the alkali-alkali spin-exchange collisions relaxation rate is shown in Fig.13.



The fundamental sensitivity of ^{39}K (^{133}Cs)- ^{85}Rb - ^{21}Ne co-magnetometers change with the number density of the buffer gas ^{21}Ne in Fig. 5(a), number density of the quench gas N_2 in Fig. 5(b), the frequency rate of pump beam in Fig. 5(c) and the power density of pump beam in Fig. 5(d), respectively.

Fig. 5(a) represents that the fundamental sensitivity of ^{39}K (^{133}Cs)- ^{85}Rb - ^{21}Ne co-magnetometer augments with the increasing number density of ^{21}Ne n_{Ne} when n_{Ne} is smaller than a critical value about $1.67 \times 10^{19} \text{ cm}^{-3}$ and decreases when n_{Ne} is bigger than the value. For this phenomenon, just as we discussed in our previous work ²⁴, we think that more alkali-metal atoms diffuse to

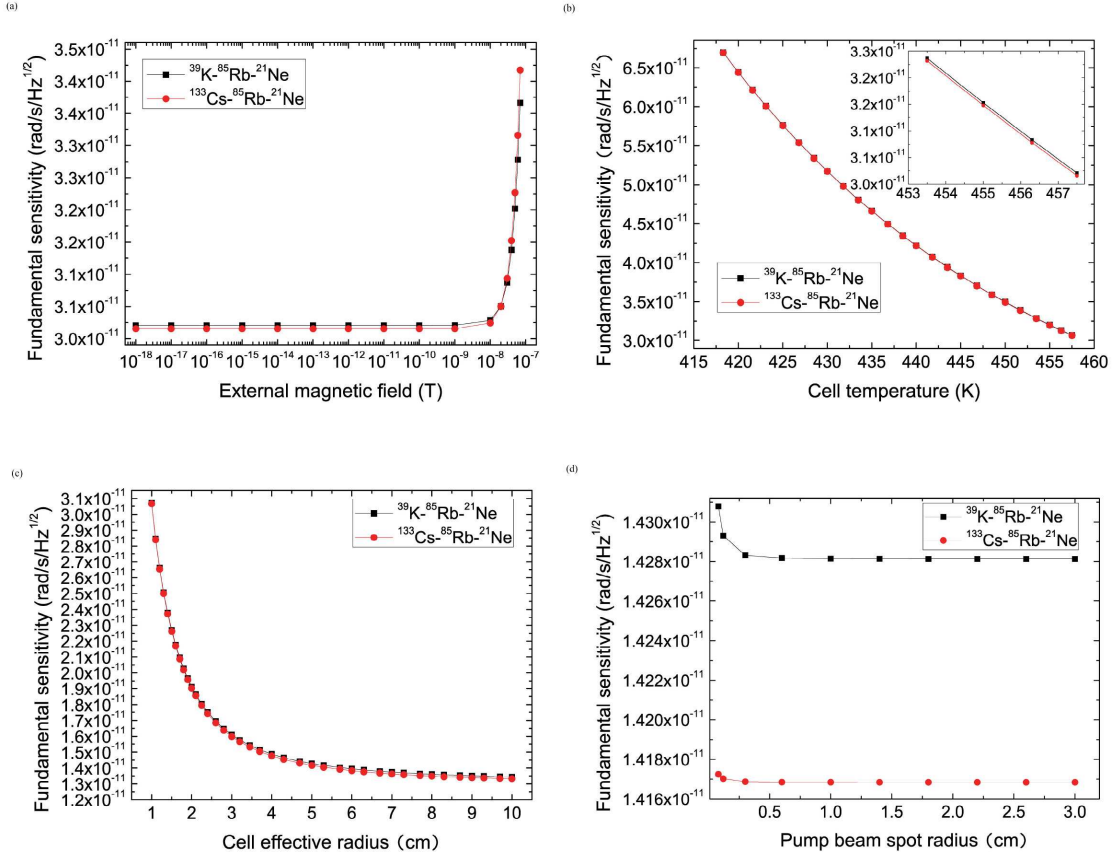
the cell wall and less spin exchange collisions between alkali-metal atoms A and B when n_{Ne} is smaller than the value and decrease. Less alkali-metal atoms diffuse to the cell wall and more spin exchange collisions between alkali-metal atoms and buffer gas so that there are less spin exchange collisions in alkali-metal atoms when n_{Ne} is bigger than the value and increase. Hence, if we take the critical value as n_{Ne} , spin exchange collisions in alkali-metal atoms are the most, we can obtain the highest fundamental sensitivity of the co-magnetometer. From equation (12), Fig. 1(a) and Fig. 8(a), we can find that R_{SD} increases with the increasing n_{Ne} , $R_{wall-K-Rb-Ne}^{Rb-Ne-N_2}$ and $R_{wall-Cs-Rb-Ne}^{Rb-Ne-N_2}$ decrease with increasing n_{Ne} , R_p^K and R_p^{Cs} increase with increasing n_{Ne} when n_{Ne} is smaller than a critical value about $3.8892 \times 10^{22} \text{ cm}^{-3}$ and $2.6214 \times 10^{23} \text{ cm}^{-3}$, respectively (which makes the R_B has the same pattern of change), other systemic parameters in the equation (12) don't change with n_{Ne} , hence, there is a smallest n_{Ne} to make the fundamental sensitivity highest, which is determined by R_{SD} , $R_{wall-K-Rb-Ne}^{Rb-Ne-N_2}$ ($R_{wall-Cs-Rb-Ne}^{Rb-Ne-N_2}$) and R_p^K (R_p^{Cs}).

Fig. 5(b) shows that the fundamental sensitivity of $^{39}\text{K}(^{133}\text{Cs})\text{-}^{85}\text{Rb}\text{-}^{21}\text{Ne}$ co-magnetometer increases with the increasing N_2 number density n_{N_2} when n_{N_2} is smaller than a critical value about $1.24 \times 10^{19} \text{ cm}^{-3}$ and decreases when n_{N_2} is higher than the value. From equation (12), Fig. 1(b), we can find that R_{SD} increases with the increasing n_{N_2} , $R_{wall-K-Rb-Ne}^{Rb-Ne-N_2}$ and $R_{wall-Cs-Rb-Ne}^{Rb-Ne-N_2}$ decrease with increasing n_{N_2} , other systemic parameters in the equation (12) don't change with n_{Ne} , hence, there is a smallest n_{N_2} to make the fundamental sensitivity highest, which is determined by R_{SD} and $R_{wall-K-Rb-Ne}^{Rb-Ne-N_2}$ ($R_{wall-Cs-Rb-Ne}^{Rb-Ne-N_2}$).

Fig. 5(c) demonstrates that when the frequency rate of pump beam is smaller than about

3.878×10^{14} Hz and 3.31×10^{14} Hz, respectively, the fundamental sensitivity of ^{39}K - ^{85}Rb - ^{21}Ne and ^{133}Cs - ^{85}Rb - ^{21}Ne co-magnetometers increase slowly, when the frequency rate is in the range 3.878×10^{14} Hz \sim 3.893×10^{14} Hz (^{85}Rb polarization is about 0.01) and 3.31×10^{14} Hz \sim 3.3475×10^{14} Hz (^{85}Rb polarization is about 0.01), the fundamental sensitivity of ^{39}K - ^{85}Rb - ^{21}Ne and ^{133}Cs - ^{85}Rb - ^{21}Ne co-magnetometers increase rapidly. The fundamental sensitivity of ^{39}K - ^{85}Rb - ^{21}Ne and ^{133}Cs - ^{85}Rb - ^{21}Ne co-magnetometers decrease rapidly when the frequency rate is in the range 3.8981×10^{14} Hz (^{85}Rb polarization is about 0.01) \sim 3.91×10^{14} Hz and 3.3597×10^{14} Hz (^{85}Rb polarization is about 0.01) \sim 3.38×10^{14} Hz respectively. When the frequency rate is bigger than about 3.91×10^{14} Hz and 3.38×10^{14} Hz respectively, the fundamental sensitivity of ^{39}K - ^{85}Rb - ^{21}Ne and ^{133}Cs - ^{85}Rb - ^{21}Ne co-magnetometers decrease slowly.

Fig. 5(d) shows that the fundamental sensitivity decreases with the increasing power density of pump beam when the power density is smaller than about 5.58×10^5 W/cm² in ^{39}K - ^{85}Rb - ^{21}Ne co-magnetometer and 1.623×10^7 W/cm² in ^{133}Cs - ^{85}Rb - ^{21}Ne co-magnetometer. Otherwise, the fundamental sensitivity will increase with the increasing power density, respectively. In the experiment, the power density is usually a few hundred mW/cm². The frequency rate and power density affect the fundamental sensitivity by changing the pumping rate of the pumping beam.



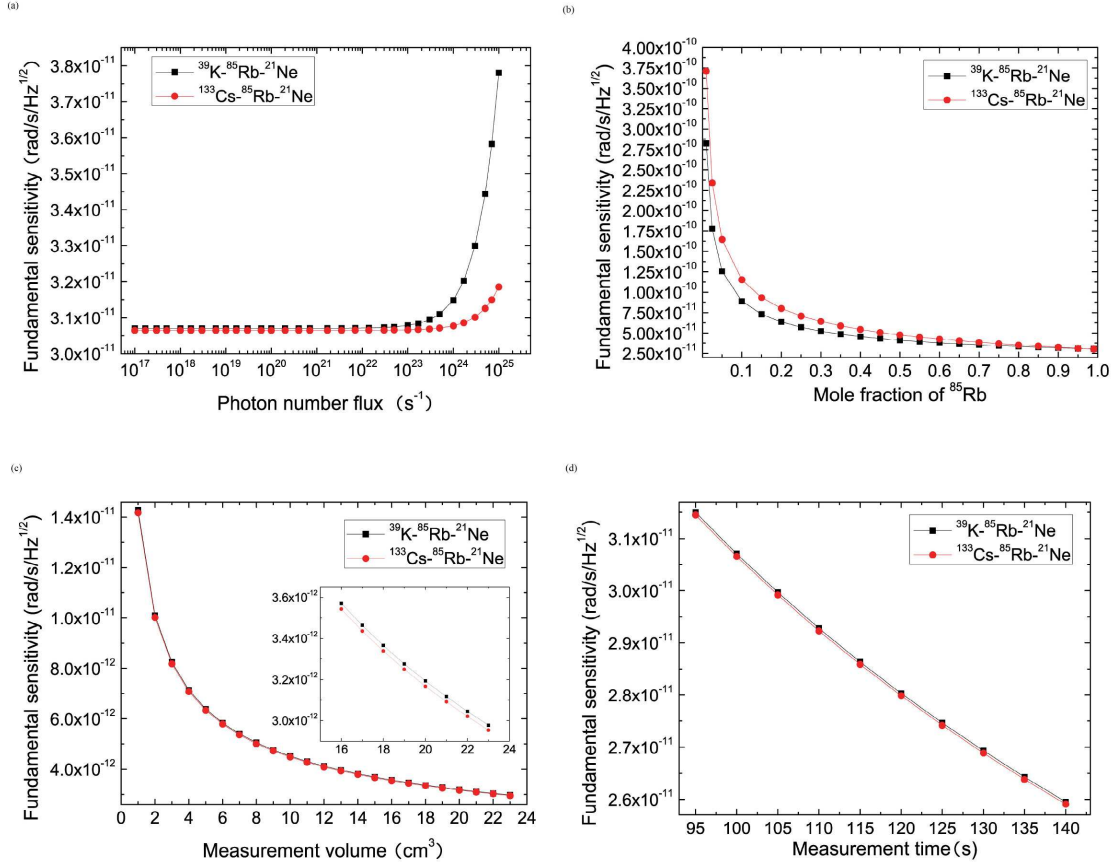
The fundamental sensitivity of ^{39}K (^{133}Cs)- ^{85}Rb - ^{21}Ne co-magnetometers change with the external magnetic field in Fig. 6(a), the cell temperature in Fig. 6(b), the cell effective radius in Fig. 6(c) and the pump beam spot radius when $a = 5\text{cm}$ in Fig. 6(d), respectively.

Fig. 6(a) describes that when the external magnetic field B is smaller than about 10^{-8} T, the fundamental sensitivity of ^{39}K (^{133}Cs)- ^{85}Rb - ^{21}Ne co-magnetometers almost do not change with the increasing B , respectively (decrease slowly). Otherwise, it decreases rapidly. When the B is smaller than about 2.0182×10^{-8} T, the fundamental sensitivity of ^{39}K - ^{85}Rb - ^{21}Ne co-magnetometer is lower than the one of ^{133}Cs - ^{85}Rb - ^{21}Ne co-magnetometer. The increasing

B will make the relaxation rate due to alkali-alkali spin-exchange collisions R_{SE}^{EE} increase and don't change other systemic parameters of equation (12), which makes the fundamental sensitivity decrease.

The fundamental sensitivity of ^{39}K (^{133}Cs)- ^{85}Rb - ^{21}Ne co-magnetometers increase with the increasing cell temperature T respectively in Fig. 6(b) and we can know that the fundamental sensitivity of ^{39}K - ^{85}Rb - ^{21}Ne co-magnetometer is lower than the one of ^{133}Cs - ^{85}Rb - ^{21}Ne co-magnetometer from the illustration. From equation (12), Fig. 1(c), Fig. 8(f) and Fig. 13(b), we can find that R_{SD} and n_B (n_{Rb}) increases with the increasing T , R_{wall} increases rapidly when the T increases and the pumping rate increases slowly with the increasing T . However, there is a larger increase for the ^{85}Rb number density and a decrease for R_{SE}^{EE} ($R_{SE}^{EE} \approx 0$) when the T increases. Hence, the fundamental sensitivity increases with the increasing T , which is mainly determined by the ^{85}Rb number density.

The fundamental sensitivity of ^{39}K (^{133}Cs)- ^{85}Rb - ^{21}Ne co-magnetometers increase with the increasing cell effective radius a , respectively in Fig. 6(c) duo to the increasing a makes the R_{wall} decrease, which will increase the fundamental sensitivity. The fundamental sensitivity of ^{39}K (^{133}Cs)- ^{85}Rb - ^{21}Ne co-magnetometers with $a = 5$ cm increase with the increasing pump beam spot radius a_p respectively in Fig. 6(d) for the increasing a_p making the pumping rate of the pump beam decrease, which will increase the fundamental sensitivity.



The fundamental sensitivity of ^{39}K (^{133}Cs)- ^{85}Rb - ^{21}Ne co-magnetometers change with the photon number flux in Fig. 7(a), mole fraction of ^{85}Rb in Fig. 7(b), the measurement volume in Fig. 7(c) and measurement time in Fig. 7(d), respectively.

Fig. 7(a) describes that the fundamental sensitivity of ^{39}K (^{133}Cs)- ^{85}Rb - ^{21}Ne co-magnetometers decrease with the increasing photon number flux Φ_{D1} and when the Φ_{D1} is lower than about 1×10^{23} /s, the fundamental sensitivity almost don't change(decrease slowly) with increasing Φ_{D1} , otherwise, the fundamental sensitivity decrease rapidly. The fundamental sensitivity increase with the increasing mole fraction of ^{85}Rb f_{Rb} respectively. When the f_{Rb} is bigger than about 0.9650,

the fundamental sensitivity of ^{133}Cs - ^{85}Rb - ^{21}Ne co-magnetometer is higher than the one of ^{39}K - ^{85}Rb - ^{21}Ne co-magnetometer in Fig. 7(b). Fig. 7(c) shows that the fundamental sensitivity of ^{39}K (^{133}Cs)- ^{85}Rb - ^{21}Ne co-magnetometers with $a = 5$ cm increase with increasing measurement volume, respectively. The fundamental sensitivity of ^{39}K (^{133}Cs)- ^{85}Rb - ^{21}Ne co-magnetometers increase with increasing measurement time respectively in Fig. 7(d).

As a result, the polarization of ^{85}Rb atom of the co-magnetometer based on ^{133}Cs - ^{85}Rb - ^{21}Ne is smaller than the one based on ^{39}K - ^{85}Rb - ^{21}Ne in Fig. 2 ~ Fig. 4 when ^{21}Ne number density is smaller than about $9.8827 \times 10^{22} \text{ cm}^{-3}$ or frequency rate of pump beam is bigger than about $3.7466 \times 10^{14} \text{ Hz}$ or the power density of pump beam is smaller than about $2.883 \times 10^6 \text{ W/cm}^2$. The fundamental sensitivity of ^{39}K - ^{85}Rb - ^{21}Ne co-magnetometer is lower than the one of ^{133}Cs - ^{85}Rb - ^{21}Ne co-magnetometer when the frequency rate of pump beam is bigger than about $3.3632 \times 10^{14} \text{ Hz}$ or smaller than about $3.3437 \times 10^{14} \text{ Hz}$, the mole fraction of ^{85}Rb is bigger than about 0.9650 or the external magnetic field is smaller than about $2.0182 \times 10^{-8} \text{ T}$ in Fig. 5 ~ Fig. 7.

We obtain a fundamental sensitivity of $3.0708 \times 10^{-10} \text{ rad/s/Hz}^{1/2}$ with ^{39}K - ^{85}Rb - ^{21}Ne co-magnetometer with ^{85}Rb polarization is 6.5324×10^{-6} and $n_K/n_{Rb} = 0.0023$, a fundamental sensitivity of $3.0655 \times 10^{-10} \text{ rad/s/Hz}^{1/2}$ with ^{133}Cs - ^{85}Rb - ^{21}Ne co-magnetometer with ^{85}Rb polarization is 1.0006×10^{-6} and $n_{Cs}/n_{Rb} = 0.0151$ when $n_{Ne} = 6 \times 10^{19} \text{ cm}^{-3}$, $n_{N2} = 2 \times 10^{17} \text{ cm}^{-3}$, $T = 457.5 \text{ K}$, $f_{Rb} = 0.97$, $\Phi_{D1}^K = \Phi_{D1}^{Cs} = 10^{20} \text{ /s}$, $I_{PI}^K = I_{PI}^{Cs} = 0.02 \text{ W/cm}^2$, $\nu_p^K = \nu_p^{Cs} = 3.99 \times 10^{14} \text{ Hz}$, $a = 1 \text{ cm}$, $a_p = 1 \text{ cm}$, $V = 1 \text{ cm}^3$, $B = 10^{-15} \text{ T}$ and $t = 1 \text{ s}$. By optimizing above parameters, we obtain a fundamental sensitivity of $3.7762 \times 10^{-12} \text{ rad/s/Hz}^{1/2}$

with ^{39}K - ^{85}Rb - ^{21}Ne with the polarization of ^{85}Rb atom is 4.7981×10^{-7} and $n_{\text{K}}/n_{\text{Rb}} = 0.0023$, a fundamental sensitivity of 3.7334×10^{-12} rad/s/Hz $^{1/2}$ with ^{133}Cs - ^{85}Rb - ^{21}Ne with the polarization of ^{85}Rb atom is 7.8163×10^{-8} and $n_{\text{Cs}}/n_{\text{Rb}} = 0.0151$ with $n_{\text{Ne}} = 1.669 \times 10^{18}$ cm $^{-3}$, $n_{\text{N}_2} = 1.2 \times 10^{18}$ cm $^{-3}$, $T = 457.5$ K, $f_{\text{Rb}} = 0.97$, $\Phi_{\text{D1}}^{\text{K}} = \Phi_{\text{D1}}^{\text{Cs}} = 10^{20}$ /s, $I_{\text{PI}}^{\text{K}} = I_{\text{PI}}^{\text{Cs}} = 0.02$ W/cm 2 , $\nu_p^{\text{K}} = \nu_p^{\text{Cs}} = 3.99 \times 10^{14}$ Hz, $a = 10$ cm, $a_p = 10$ cm, $V = 1000$ cm 3 , $B = 10^{-15}$ T and $t = 1$ s, with higher fundamental sensitivity possible at bigger measurement volume, proper amount of buffer gas and quench gas, smaller pumping rate of pump beam, higher temperature and longer measurement time.

Discussion

In conclusion, we find that the ^{85}Rb polarization of ^{133}Cs - ^{85}Rb - ^{21}Ne co-magnetometer is bigger than the one of ^{39}K - ^{85}Rb - ^{21}Ne co-magnetometer when ^{21}Ne number density is bigger than about 9.8827×10^{22} cm $^{-3}$, frequency rate of pump beam is smaller than about 3.7466×10^{14} Hz or the power density of pump beam is bigger than about 2.883×10^6 W/cm 2 . The fundamental sensitivity of ^{133}Cs - ^{85}Rb - ^{21}Ne co-magnetometer is higher than the one of ^{39}K - ^{85}Rb - ^{21}Ne co-magnetometer when the frequency rate of pump beam is bigger than about 3.3632×10^{14} Hz or smaller than about 3.3437×10^{14} Hz, or the external magnetic field is smaller than about 2.0182×10^{-8} T, or mole fraction of ^{85}Rb is bigger than about 0.9650.

In practical applications, we have considered some questions in our previous work about ^{39}K (^{133}Cs)- ^{85}Rb - ^4He hybrid optical pumping SERF atomic magnetometers²⁴, which are suited to the conditions of ^{39}K (^{133}Cs)- ^{85}Rb - ^{21}Ne co-magnetometers: the minimum total number of atoms

Table 1: Parameters used for the calculation

<i>parameter</i>	<i>value</i>
Boltzmann's constant k_B	1.38×10^{-23} J/K
Atomic mass unit m	$1.660539040(20) \times 10^{-27}$ kg
π	3.14
^{21}Ne nuclear gyromagnetic ratio 59	2.1×10^7 rad/s/T
Electron spin g factor	2×1.001159657
Planck's constant \hbar	1.054589×10^{-34} Js
Bohr magneton μ_B	9.27408×10^{-24} J/T
The mole fraction of ^{39}K	0.03
The mole fraction of ^{133}Cs	0.03
$D_0(K - \text{Ne})$ 39	$0.19 \text{ cm}^2/\text{s}$
$D_0(\text{Rb} - \text{Ne})$ 41	$0.2 \text{ cm}^2/\text{s}$
$D_0(\text{Cs} - \text{Ne})$ 40	$0.171 \text{ cm}^2/\text{s}$
$D_0(K - \text{N}_2)$ 42	$0.2 \text{ cm}^2/\text{s}$
$D_0(\text{Rb} - \text{N}_2)$ 41	$0.19 \text{ cm}^2/\text{s}$
$D_0(\text{Cs} - \text{N}_2)$ 40	$0.098 \text{ cm}^2/\text{s}$
σ_{SE}^K 55	$1.8 \times 10^{-14} \text{ cm}^2$
σ_{SE}^{Rb} 52	$1.9 \times 10^{-14} \text{ cm}^2$
σ_{SE}^{Cs} 52	$2.1 \times 10^{-14} \text{ cm}^2$
σ_{SD}^K 62	$1 \times 10^{-18} \text{ cm}^2$
σ_{SD}^{Rb} 46	$1.6 \times 10^{-17} \text{ cm}^2$
σ_{SD}^{Cs} 63	$2 \times 10^{-16} \text{ cm}^2$
$\sigma_{SE}^{K-\text{Rb}}$ 24	$\sigma_{SE}^K \frac{n_K}{n_K+n_{\text{Rb}}} + \sigma_{SE}^{\text{Rb}} \frac{n_{\text{Rb}}}{n_K+n_{\text{Rb}}}$
$\sigma_{SE}^{\text{Rb}-K}$ 24	$\sigma_{SE}^{\text{Rb}} \frac{n_{\text{Rb}}}{n_K+n_{\text{Rb}}} + \sigma_{SE}^K \frac{n_K}{n_K+n_{\text{Rb}}}$
$\sigma_{SE}^{\text{Cs}-\text{Rb}}$ 24	$\sigma_{SE}^{\text{Cs}} \frac{n_{\text{Cs}}}{n_{\text{Cs}}+n_{\text{Rb}}} + \sigma_{SE}^{\text{Rb}} \frac{n_{\text{Rb}}}{n_{\text{Cs}}+n_{\text{Rb}}}$
$\sigma_{SE}^{\text{Rb}-\text{Cs}}$ 24	$\sigma_{SE}^{\text{Rb}} \frac{n_{\text{Rb}}}{n_{\text{Cs}}+n_{\text{Rb}}} + \sigma_{SE}^{\text{Cs}} \frac{n_{\text{Cs}}}{n_{\text{Cs}}+n_{\text{Rb}}}$
$\sigma_{SE}^{^{87}\text{Rb}-^{133}\text{Cs}}$ 51	$(2.3 \pm 0.2) \times 10^{-14} \text{ cm}^2$
$\sigma_{SD}^{K-\text{Rb}}$	$\sigma_{SD}^K \frac{n_K}{n_K+n_{\text{Rb}}} + \sigma_{SD}^{\text{Rb}} \frac{n_{\text{Rb}}}{n_K+n_{\text{Rb}}}$
$\sigma_{SD}^{\text{Rb}-K}$	$\sigma_{SD}^{\text{Rb}} \frac{n_{\text{Rb}}}{n_K+n_{\text{Rb}}} + \sigma_{SD}^K \frac{n_K}{n_K+n_{\text{Rb}}}$
$\sigma_{SD}^{\text{Cs}-\text{Rb}}$	$\sigma_{SD}^{\text{Cs}} \frac{n_{\text{Cs}}}{n_{\text{Cs}}+n_{\text{Rb}}} + \sigma_{SD}^{\text{Rb}} \frac{n_{\text{Rb}}}{n_{\text{Cs}}+n_{\text{Rb}}}$
$\sigma_{SD}^{\text{Rb}-\text{Cs}}$	$\sigma_{SD}^{\text{Rb}} \frac{n_{\text{Rb}}}{n_{\text{Cs}}+n_{\text{Rb}}} + \sigma_{SD}^{\text{Cs}} \frac{n_{\text{Cs}}}{n_{\text{Cs}}+n_{\text{Rb}}}$
$\sigma_{SD}^{K-\text{Ne}}$ 36,39	$1 \times 10^{-23} \text{ cm}^2$
$\sigma_{SD}^{\text{Rb}-\text{Ne}}$ 56	$5.2 \times 10^{-23} \text{ cm}^2$
$\sigma_{SD}^{\text{Cs}-\text{Ne}}$ 57	$1 \times 10^{-22} \text{ cm}^2$
$\sigma_{SD}^{K-\text{N}_2}$ 27,58	$7.9 \times 10^{-23} \text{ cm}^2$
$\sigma_{SD}^{\text{Rb}-\text{N}_2}$ 27,36	$1 \times 10^{-22} \text{ cm}^2$
$\sigma_{SD}^{\text{Cs}-\text{N}_2}$ 27,36	$5.5 \times 10^{-22} \text{ cm}^2$
Nuclear Spin of ^{39}K I_K	1.5
Nuclear Spin of ^{85}Rb I_{Rb}	2.5
Nuclear Spin of ^{133}Cs I_{Cs}	3.5

necessary for the operation of the magnetometer with the desired accuracy, as well as the geometric size of the setup - how small can it be made? How does the fundamental sensitivity of the elaborated setup depend on the number of atoms?

Firstly, we can find that when number density of alkali-metal atom (which is determined by the mole fraction and the cell temperature for the hybrid vapor cell with two types of alkali-metal atoms), buffer gas and quench gas are certain, if we also know the effective radius of vapor cell, pump beam spot radius, frequency rate of pump beam, photon number flux, power density of pump beam, external magnetic field, measurement volume and measurement time, we can obtain the corresponding total number of the atoms and the fundamental sensitivity of the co-magnetometers. Because the number density of alkali-metal atom is determined by the cell temperature and the mole fraction for the hybrid vapor cell with two types of alkali-metal atoms, we can find that how the fundamental sensitivity of the co-magnetometer depend on the number density of alkali-metal atom, buffer gas and quench gas from Fig. 5(a), Fig. 5(b) and Fig. 6(b) (the cell temperature and the mole fraction corresponds to the number density of alkali metal atoms). The less number density of buffer gas and quench gas, the bigger R_{wall} , it's hard to say the minimum number density of buffer gas and quench gas, but we find that there are critical values for the number density of buffer gas and quench gas to make the fundamental sensitivity of the co-magnetometers highest.

Secondly, the smallest geometric size of the setup and volume of vapor cell depends on the processing method and materials. For example, the sensitivity of the atomic spin gyroscope based on comagnetometer with ^{21}Ne atoms and a measurement volume of around 150 cm^3 is 1.2×10^{-9}

$^{\circ}/\text{s}/\text{Hz}^{1/2}$ (an equal angular random walk of $7.2 \times 10^{-8} \text{ }^{\circ}/\text{h}^{1/2}$), which indicates that this type of atomic spin gyroscope has outstanding advantages of high sensitivity and compact size^{27,59}.

Thirdly, the alkali-metal atoms in the vapor cell are operated in the “hot-gas” regime. If the atomic gas is cooled to the state of a Bose-Einstein condensation (BEC), the operation may be essentially improved. For example, Dutta et al. reported the operation of a cold-atom inertial sensor which continuously captures the rotation signal, demonstrated a rotation sensitivity of 100 nrad/s/Hz^{1/2} in a cold-atom gyroscope of 11 cm² Sagnac area and a rotation stability of 1 nrad/s at 10⁴ s of integration time, which represents the state of the art for atomic gyroscopes⁶⁴. Hence, we can use cold atom gyroscope to obtain higher sensitivity of inertia measurement, which is very important for the application of the cold atom gyroscope in the field of navigation.

To obtain a higher fundamental sensitivity between ³⁹K-⁸⁵Rb-²¹Ne and ¹³³Cs-⁸⁵Rb-²¹Ne co-magnetometers, we should choose ¹³³Cs-⁸⁵Rb-²¹Ne co-magnetometer (when the frequency rate of pump beam is bigger than about 3.3632×10^{14} Hz or smaller than about 3.3437×10^{14} Hz, or the mole fraction of ⁸⁵Rb is bigger than about 0.9650) or the external magnetic field is smaller than about 2.0182×10^{-8} T with ²¹Ne atoms as the buffer gas and take the critical value of ²¹Ne number density and quench gas N₂ number density, increase the cell effective radius, the pump beam spot radius, the measurement volume, the cell temperature (when the quantity of alkali-metal atoms are enough), the measurement time and mole fraction of ⁸⁵Rb atoms, reduce the external magnetic field and photon number flux, choose suitable frequency rate of pump beam and power density of pump beam based on actual demand of the fundamental sensitivity and spatial

resolution. We estimate the fundamental sensitivity limit of the co-magnetometers due to the shot-noise superior to 3.7334×10^{-12} rad/s/Hz^{1/2} with ¹³³Cs-⁸⁵Rb-²¹Ne co-magnetometer, which is higher than the one of a K-²¹Ne atomic co-magnetometer of 2×10^{-10} rad/s/Hz^{1/2}. We could choose suitable conditions on the basis of the experiment requirements to gain a higher sensitivity of the co-magnetometers, keep the costs down and carry forward the miniaturization and practical application of the co-magnetometers.

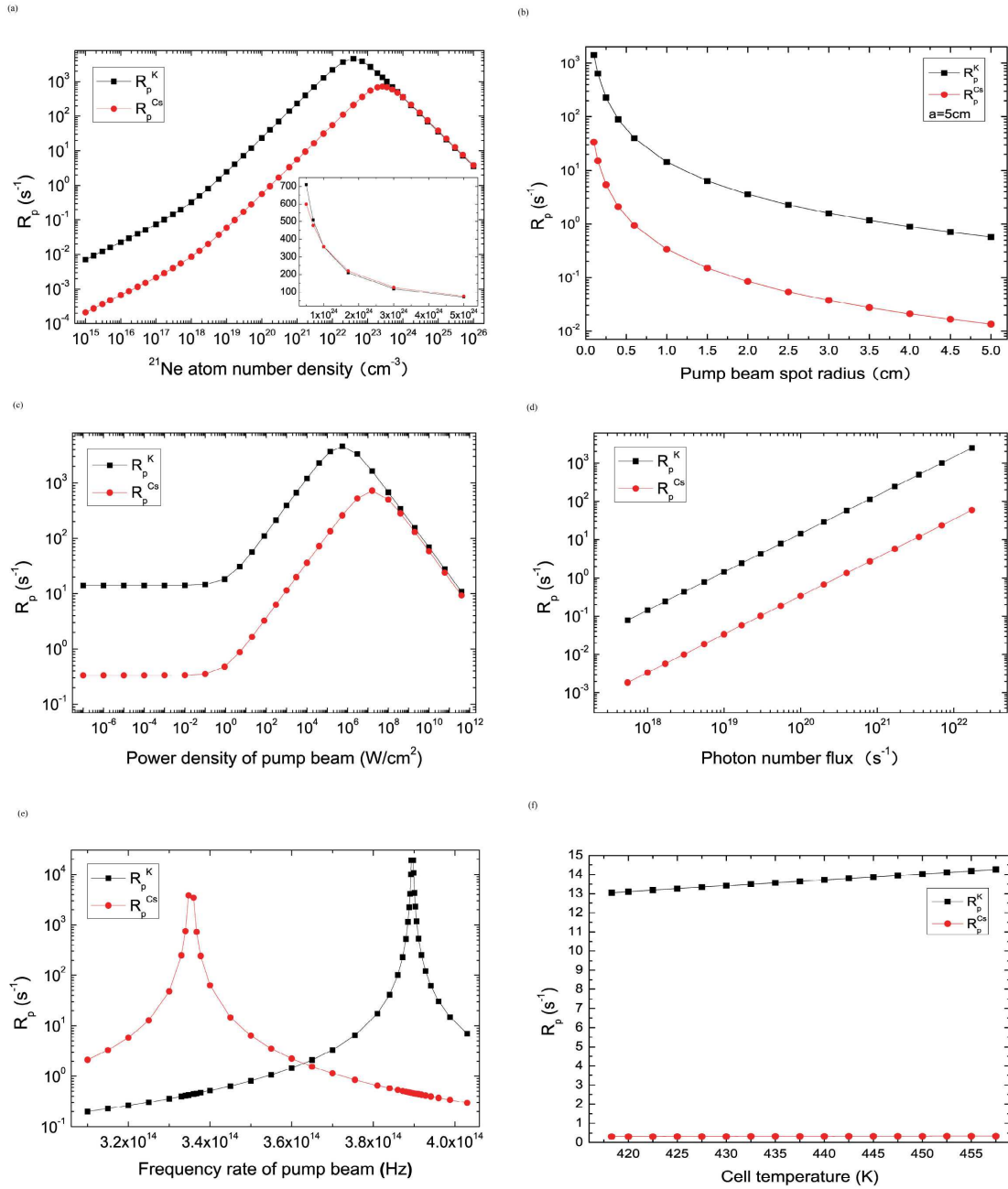
Methods

The calculation details of polarization and fundamental sensitivity. Because the slowing factors are different in the polarization of ³⁹K-⁸⁵Rb-²¹Ne and ¹³³Cs-⁸⁵Rb-²¹Ne co-magnetometers, we take the slowing factors at a low polarization limit for the convenience of theoretical analysis. The number density of the ²¹Ne, the photon number flux, the pump beam spot radius and the frequency rate will affect the polarization greatly by affecting the the pumping rate of pump beam. We systematically studied the variations of the pumping rate of pump beam, frequency shift, B^n , B^e , the relaxation rate for alkali-alkali spin-exchange collisions. We get above results by MATLAB and take several points to plot with Origin 8.

1 The variations of the pumping rate of pump beam

In this section, we calculated the variation of the pumping rate of pump beam of ³⁹K R_p^K in ³⁹K-⁸⁵Rb-²¹Ne co-magnetometer and the pumping rate of pump beam of ¹³³Cs R_p^{Cs} in ¹³³Cs-⁸⁵Rb-²¹Ne co-magnetometer with the number density of the buffer gas ²¹Ne n_{Ne} , the pump beam spot radius a_p , the power density of pump beam I_{PI} , the photon number flux Φ_{D1} , the frequency rate of pump

beam ν_p and the cell temperature T , respectively.



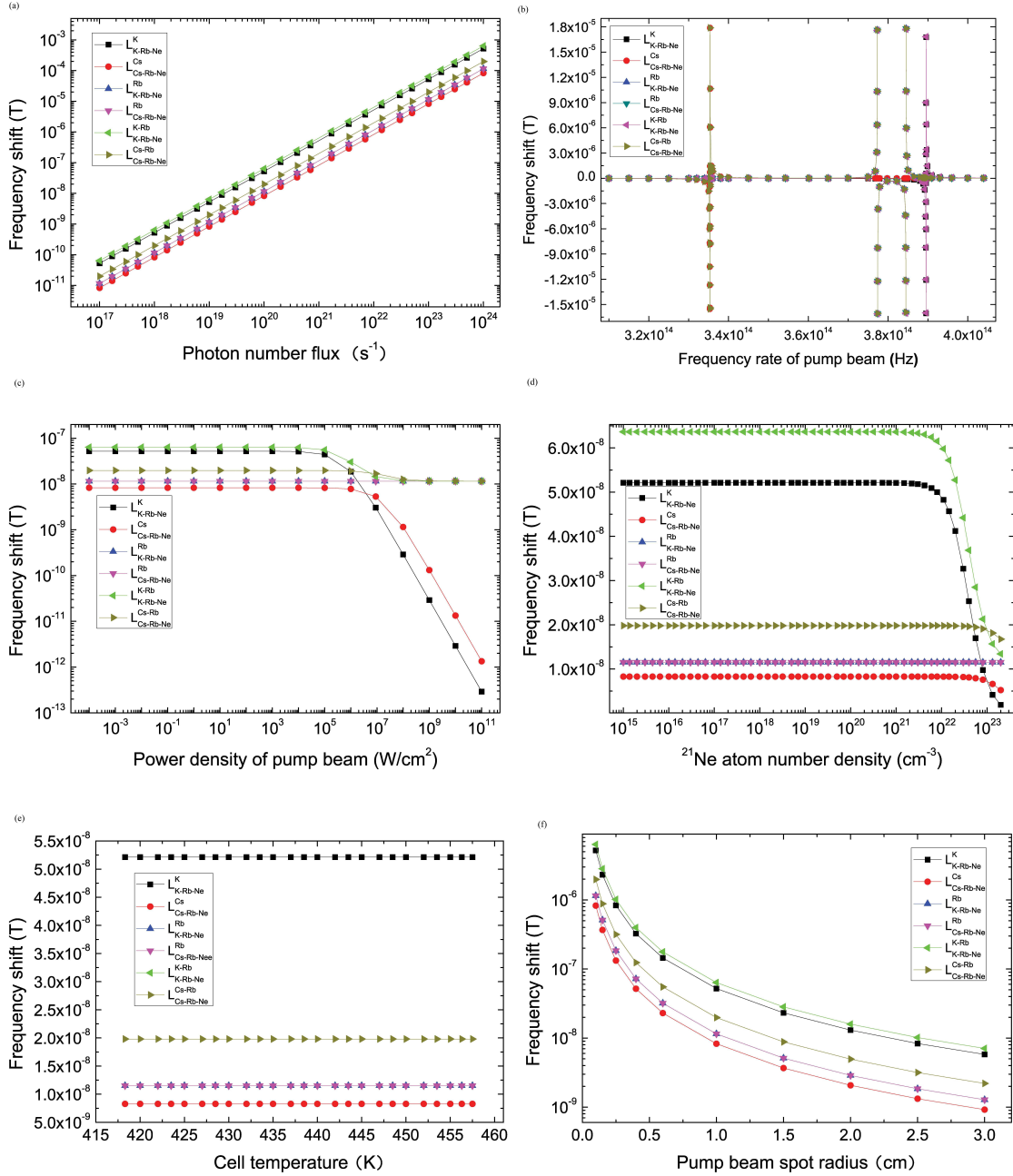
The pumping rate of pump beam of ³⁹K R_p^K in ³⁹K-⁸⁵Rb-²¹Ne co-magnetometer and the pumping rate of pump beam of ¹³³Cs R_p^{Cs} in ¹³³Cs-⁸⁵Rb-²¹Ne co-magnetometer change with

n_{Ne} in Fig. 8(a), a_p when $a = 5\text{cm}$ in Fig. 8(b), I_{PI} in Fig. 8(c), Φ_{D1} in Fig. 8(d), ν_p in Fig. 8(e) and T in Fig. 8(f), respectively.

Fig. 8(a) shows that the R_p^K and R_p^{Cs} increase with the increasing n_{Ne} when n_{Ne} is smaller than a critical value about $3.8892 \times 10^{22} \text{ cm}^{-3}$ and $2.6214 \times 10^{23} \text{ cm}^{-3}$, respectively. Otherwise, R_p^K and R_p^{Cs} decrease with increasing n_{Ne} . Fig. 8(b) demonstrates that R_p^K and R_p^{Cs} decrease with increasing a_p when $a = 5\text{cm}$. Fig. 8(c) shows that R_p^K and R_p^{Cs} increase with the increasing I_{PI} when the I_{PI} is smaller than a critical value about $5.499 \times 10^5 \text{ W/cm}^2$ and $1.6156 \times 10^7 \text{ W/cm}^2$, respectively. Otherwise, R_p^K and R_p^{Cs} decrease with the increasing I_{PI} .

Fig. 8(d) shows that R_p^K and R_p^{Cs} increase with the increasing Φ_{D1} . Fig. 8(e) demonstrates that R_p^K and R_p^{Cs} increase with the increasing ν_p when the ν_p is smaller than a critical value about $3.8956 \times 10^{14} \text{ Hz}$ and $3.3535 \times 10^{14} \text{ Hz}$, respectively. Otherwise, R_p^K and R_p^{Cs} decrease with the increasing ν_p . Fig. 8(f) shows that R_p^K and R_p^{Cs} increase with increasing T , due to the increasing T increases the linewidth of the K-Ne and Cs-Ne pressure broadening, which make R_p^K and R_p^{Cs} increase.

The variations of frequency shift



The frequency shifts change with the photon number flux in Fig. 9(a), frequency rate of pump beam in Fig. 9(b), power density of pump beam in Fig. 9(c), the ^{21}Ne number density in Fig. 9(d), cell temperature in Fig. 9(e) and pump beam spot radius when $a = 5cm$ in Fig.

9(f), respectively.

In this section, we calculated the variation of the frequency shift of ^{39}K atoms $L_{K-Rb-Ne}^K$, the frequency shift of ^{85}Rb atoms $L_{K-Rb-Ne}^{Rb}$ and their sum $L_{K-Rb-Ne}^{KRb}$ in ^{39}K - ^{85}Rb - ^{21}Ne co-magnetometer, the frequency shift of ^{133}Cs atoms $L_{Cs-Rb-Ne}^{Cs}$, the frequency shift of ^{85}Rb atoms $L_{Cs-Rb-Ne}^{Rb}$ and their sum $L_{Cs-Rb-Ne}^{CsRb}$ in ^{133}Cs - ^{85}Rb - ^{21}Ne co-magnetometer with the photon number flux Φ_{D1} , the frequency rate of pump beam ν_p , the power density of pump beam I_{PI} , the ^{21}Ne number density n_{Ne} , the cell temperature T and the pump beam spot radius a_p , respectively.

Fig. 9(a) shows that the frequency shift increases with increasing Φ_{D1} . Fig. 9(b) demonstrates that $L_{K-Rb-Ne}^K$ decreases with increasing ν_p when the ν_p is smaller than about 3.8954×10^{14} Hz and bigger than about 3.8957×10^{14} Hz, otherwise, $L_{K-Rb-Ne}^K$ increases. $L_{Cs-Rb-Ne}^{Cs}$ decreases with increasing ν_p when the ν_p is smaller than about 3.3533×10^{14} Hz and bigger than about 3.3536×10^{14} Hz, otherwise, $L_{Cs-Rb-Ne}^{Cs}$ increases. $L_{K-Rb-Ne}^{Rb}$ increases with increasing ν_p when the ν_p is smaller than about 3.7735×10^{14} Hz. When the ν_p is in the range about 3.7736×10^{14} Hz \sim 3.8093×10^{14} Hz, $L_{K-Rb-Ne}^{Rb}$ and $L_{K-Rb-Ne}^{K-Rb}$ are negative and increase. When the ν_p is in the range 3.8094×10^{14} Hz \sim 3.8451×10^{14} Hz, $L_{K-Rb-Ne}^{Rb}$ and $L_{K-Rb-Ne}^{K-Rb}$ are negative and decrease. When the ν_p is bigger than about 3.8452×10^{14} Hz, $L_{K-Rb-Ne}^{Rb}$ is positive and decreases. $L_{K-Rb-Ne}^{K-Rb}$ is negative and decreases when the ν_p is smaller than about 3.5429×10^{14} Hz. When the ν_p is in the range 3.5429×10^{14} Hz \sim 3.7735×10^{14} Hz, $L_{K-Rb-Ne}^{K-Rb}$ increases with increasing ν_p . When the ν_p is in the range about 3.8452×10^{14} Hz \sim 3.8954×10^{14} Hz, $L_{K-Rb-Ne}^{K-Rb}$ decreases. When the ν_p is in the range about 3.8955×10^{14} Hz \sim 3.8957×10^{14} Hz, $L_{K-Rb-Ne}^{K-Rb}$ increases. When the ν_p is bigger

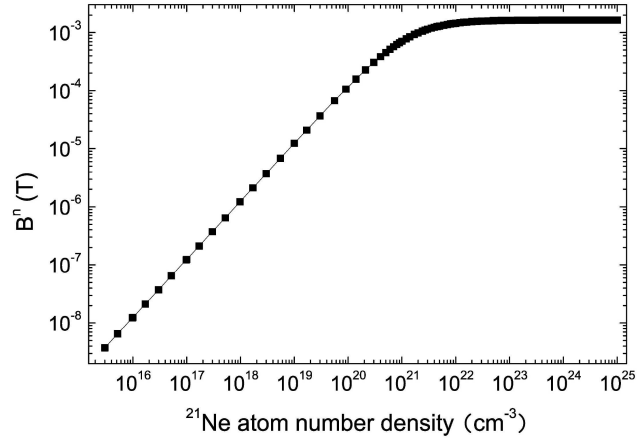
than about 3.8957×10^{14} Hz, $L_{K-Rb-Ne}^{K-Rb}$ decreases. $L_{Cs-Rb-Ne}^{Cs-Rb}$ decreases with increasing ν_p when the ν_p is in the range about 3.1×10^{14} Hz \sim 3.3533×10^{14} Hz and 3.3536×10^{14} Hz \sim 3.6017×10^{14} Hz, 3.8094×10^{14} Hz \sim 3.8451×10^{14} Hz, 3.8452×10^{14} Hz \sim 4.04×10^{14} Hz. $L_{Cs-Rb-Ne}^{Cs-Rb}$ increases when the ν_p is in the range about 3.3534×10^{14} Hz \sim 3.3536×10^{14} Hz, 3.6017×10^{14} Hz \sim 3.7735×10^{14} Hz and 3.7736×10^{14} Hz \sim 3.8093×10^{14} Hz.

Fig. 9(c) shows that $L_{K-Rb-Ne}^K$ and $L_{Cs-Rb-Ne}^{Cs}$ decrease slowly with increasing I_{PI} when the I_{PI} is smaller than about 10^5 W/cm² and 10^6 W/cm² respectively, otherwise, $L_{K-Rb-Ne}^K$ and $L_{Cs-Rb-Ne}^{Cs}$ decrease rapidly. $L_{K-Rb-Ne}^{Rb}$ and $L_{Cs-Rb-Ne}^{Rb}$ don't change with the I_{PI} for $L_{K-Rb-Ne}^{Rb}$ and $L_{Cs-Rb-Ne}^{Rb}$ have nothing to do with the I_{PI} . $L_{K-Rb-Ne}^{K-Rb}$ and $L_{Cs-Rb-Ne}^{Cs-Rb}$ decrease with the increasing I_{PI} .

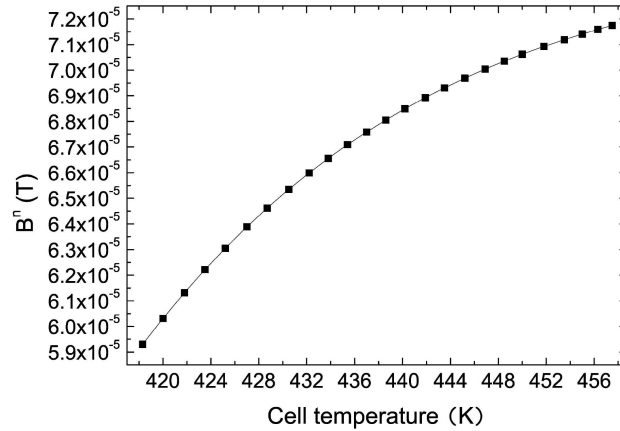
Fig. 9(d) demonstrates that $L_{K-Rb-Ne}^K$ and $L_{K-Rb-Ne}^{K-Rb}$, $L_{Cs-Rb-Ne}^{Cs}$ and $L_{Cs-Rb-Ne}^{Cs-Rb}$ decrease slowly with increasing n_{Ne} when the n_{Ne} is smaller than about 6×10^{21} cm⁻³ and 5.6×10^{22} cm⁻³, respectively, otherwise, they decrease rapidly. $L_{K-Rb-Ne}^{Rb}$ and $L_{Cs-Rb-Ne}^{Rb}$ don't change with the n_{Ne} for $L_{K-Rb-Ne}^{Rb}$ and $L_{Cs-Rb-Ne}^{Rb}$ have nothing to do with the n_{Ne} . Fig. 9(e) shows that $L_{K-Rb-Ne}^K$, $L_{Cs-Rb-Ne}^{Cs}$, $L_{K-Rb-Ne}^{K-Rb}$ and $L_{Cs-Rb-Ne}^{Cs-Rb}$ decrease slowly with increasing T , duo to the increasing T increases the linewidth of the K-Ne and Cs-Ne pressure broadening, which make $L_{K-Rb-Ne}^K$, $L_{Cs-Rb-Ne}^{Cs}$, $L_{K-Rb-Ne}^{K-Rb}$ and $L_{Cs-Rb-Ne}^{Cs-Rb}$ decrease. However, $L_{K-Rb-Ne}^{Rb}$ and $L_{Cs-Rb-Ne}^{Rb}$ don't change with the T for $L_{K-Rb-Ne}^{Rb}$ and $L_{Cs-Rb-Ne}^{Rb}$ have nothing to do with the T . Fig. 9(f) demonstrates that the frequency shift decreases with the increasing a_p when $a = 5$ cm, which affects the transverse area of the pumping light A_t .

The variations of B^n

(a)



(b)

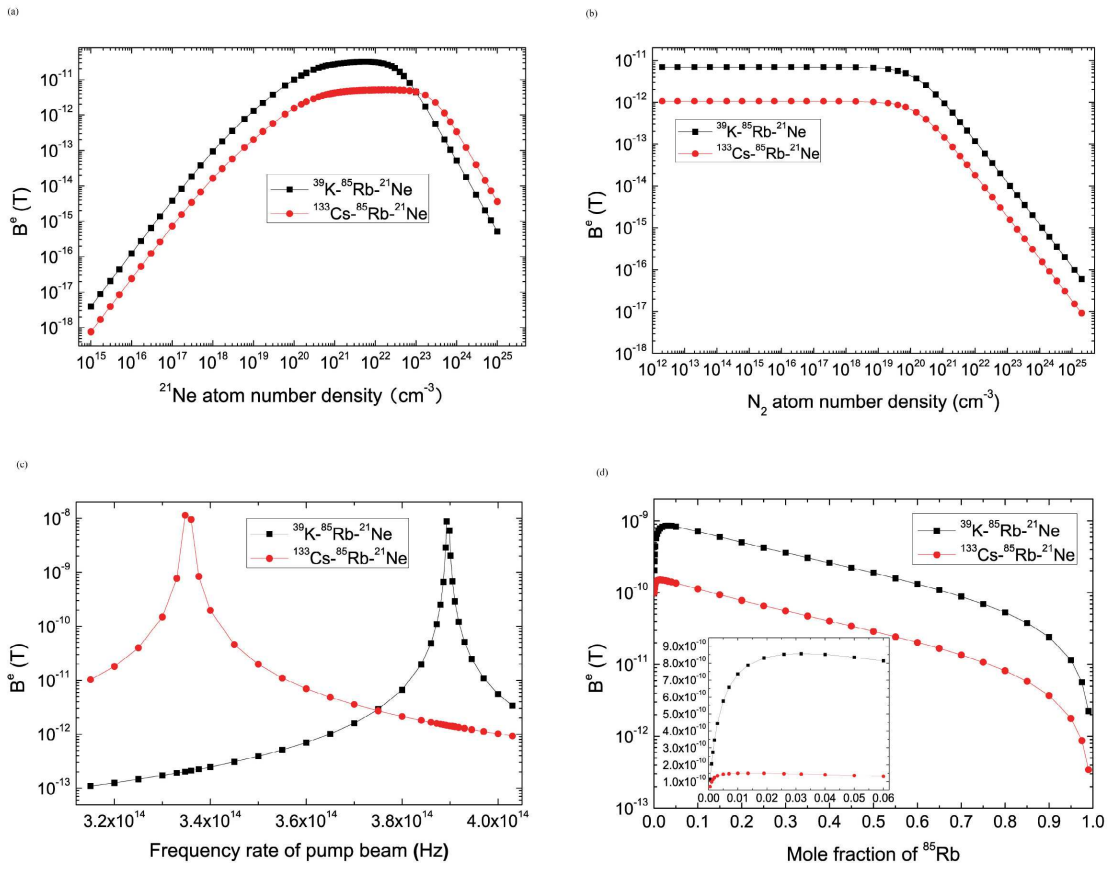


The magnetic field B^n , which is produced by the ^{21}Ne atom spins through spin-exchange interaction with ^{85}Rb atom spins, changes with ^{21}Ne number density in Fig. 10(a) and cell temperature in Fig. 10(b), respectively.

The magnetic field B^n , which is produced by the ^{21}Ne atoms spins through spin-exchange interaction with ^{85}Rb atoms spins, increases rapidly when ^{21}Ne number density is smaller than

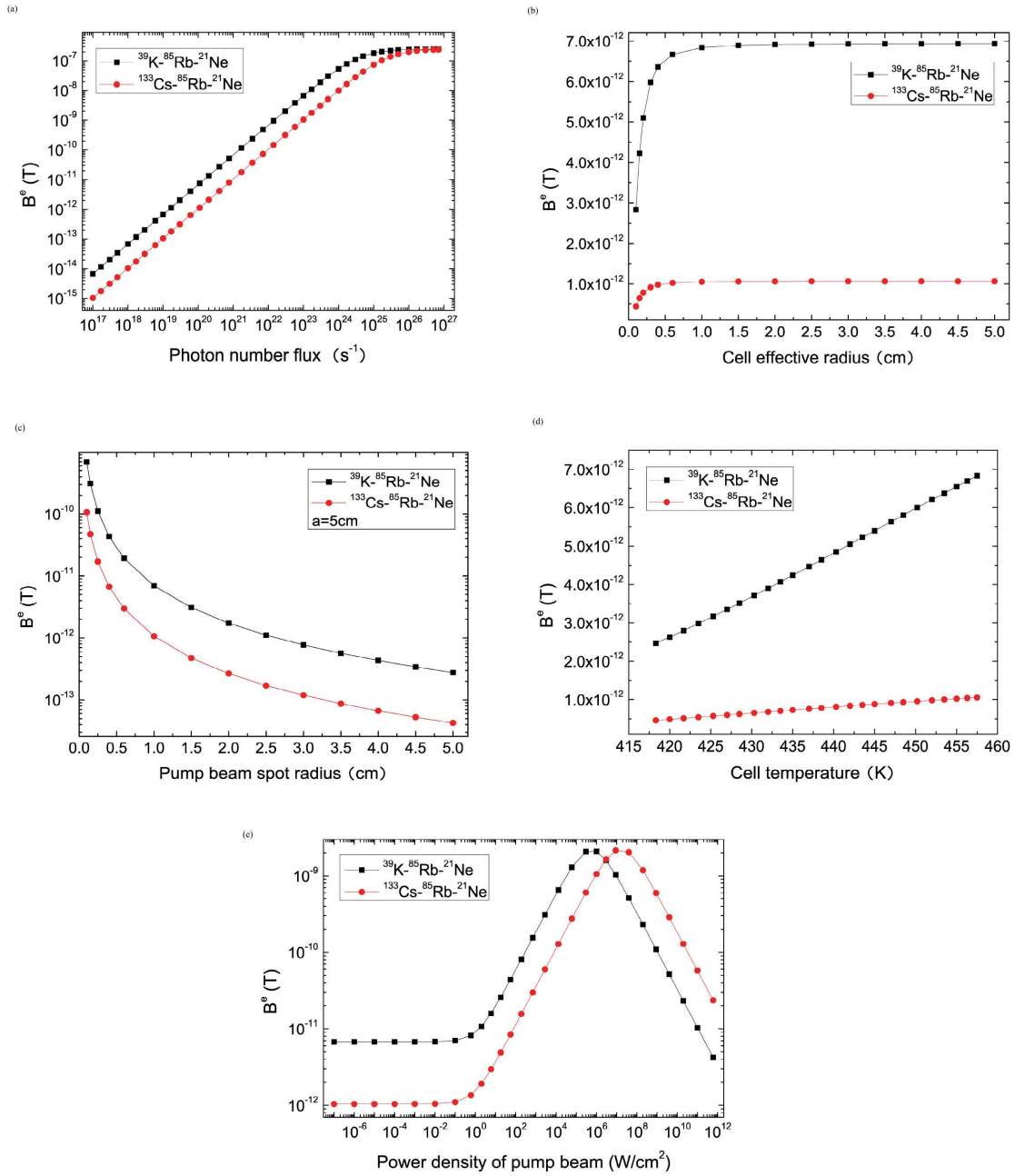
about $4.0 \times 10^{22} \text{ cm}^{-3}$, then increases slowly and tends to a constant in Fig. 10(a) from the equation of B^n and T_{1n} . Fig. 10(b) shows that B^n increases with increasing cell temperature T and B^n tends to a constant in the end duo to only R_{Rb-Ne}^{sc} changes with the T from the equation of B^n and R_{Rb-Ne}^{sc} increases with the increasing T .

The variations of B^e



The magnetic field B^e , which is experienced by the ^{21}Ne spins and produced by Rb atom spins, changes with ^{21}Ne number density in Fig. 11(a), N_2 number density in Fig. 11(b), the frequency rate of pump beam in Fig. 11(c) and mole fraction of ^{85}Rb in Fig. 11(d),

respectively.



B^e changes with the photon number flux in Fig. 12(a), cell effective radius in Fig. 12(b), the pump beam spot radius when $a = 5\text{cm}$ in Fig. 12(c), the cell temperature in Fig. 12(d) and

the power density of pump beam in Fig. 12(e), respectively.

In this section, we can find that the magnetic field B^e , which is experienced by the ^{21}Ne atoms spins and produced by Rb atoms spins, increases with the increasing ^{21}Ne number density n_{N_e} when n_{N_e} is smaller than about $5.6071 \times 10^{21} \text{ cm}^{-3}$ in ^{39}K - ^{85}Rb - ^{21}Ne and $2.01 \times 10^{22} \text{ cm}^{-3}$ in ^{133}Cs - ^{85}Rb - ^{21}Ne co-magnetometer respectively, then decreases in Fig. 11(a). From the equation of B^e , P_{zRb}^e and R_{SD} , Fig. 1(a) and Fig. 8(a), we can find that $R_{wall-K-Rb-N_e}^{Rb-Ne-N_2}$ and $R_{wall-Cs-Rb-N_e}^{Rb-Ne-N_2}$ decrease with increasing n_{N_e} , R_{SD} increases with the increasing n_{N_e} , R_p^K and R_p^{Cs} increase with the increasing n_{N_e} when n_{N_e} is smaller than a critical value about $3.8892 \times 10^{22} \text{ cm}^{-3}$ and $2.6214 \times 10^{23} \text{ cm}^{-3}$, respectively (which makes the R_B (R_{Rb}) has the same pattern of change), then decrease. Other systemic parameters don't change with n_{N_e} , hence, there is a critical value for n_{N_e} to make the P_{zRb}^e biggest, which makes the B^e biggest. Fig. 11(b) shows that B^e decreases slowly when N_2 number density n_{N_2} is smaller than about $4.0 \times 10^{19} \text{ cm}^{-3}$ in ^{39}K - ^{85}Rb - ^{21}Ne and ^{133}Cs - ^{85}Rb - ^{21}Ne co-magnetometer respectively, then begin to decrease rapidly. From the equation of B^e , P_{zRb}^e and R_{SD} , Fig. 1(b), there are only R_{SD} and $R_{wall-K-Rb-N_e}^{Rb-Ne-N_2}$ and $R_{wall-Cs-Rb-N_e}^{Rb-Ne-N_2}$ changing with n_{N_2} . R_{SD} increases with the increasing n_{N_2} , $R_{wall-K-Rb-N_e}^{Rb-Ne-N_2}$ and $R_{wall-Cs-Rb-N_e}^{Rb-Ne-N_2}$ decrease with increasing n_{N_2} , the increasing magnitude of R_{SD} is bigger than the the decreasing magnitude of $R_{wall-K-Rb-N_e}^{Rb-Ne-N_2}$ and $R_{wall-Cs-Rb-N_e}^{Rb-Ne-N_2}$, which makes P_{zRb}^e decrease, at the same time, B^e decreases with the increasing n_{N_2} .

B^e increases with the increasing frequency rate of pump beam ν_p when the ν_p is smaller than about $3.8955 \times 10^{14} \text{ Hz}$ in ^{39}K - ^{85}Rb - ^{21}Ne and $3.3534 \times 10^{14} \text{ Hz}$ in ^{133}Cs - ^{85}Rb - ^{21}Ne co-

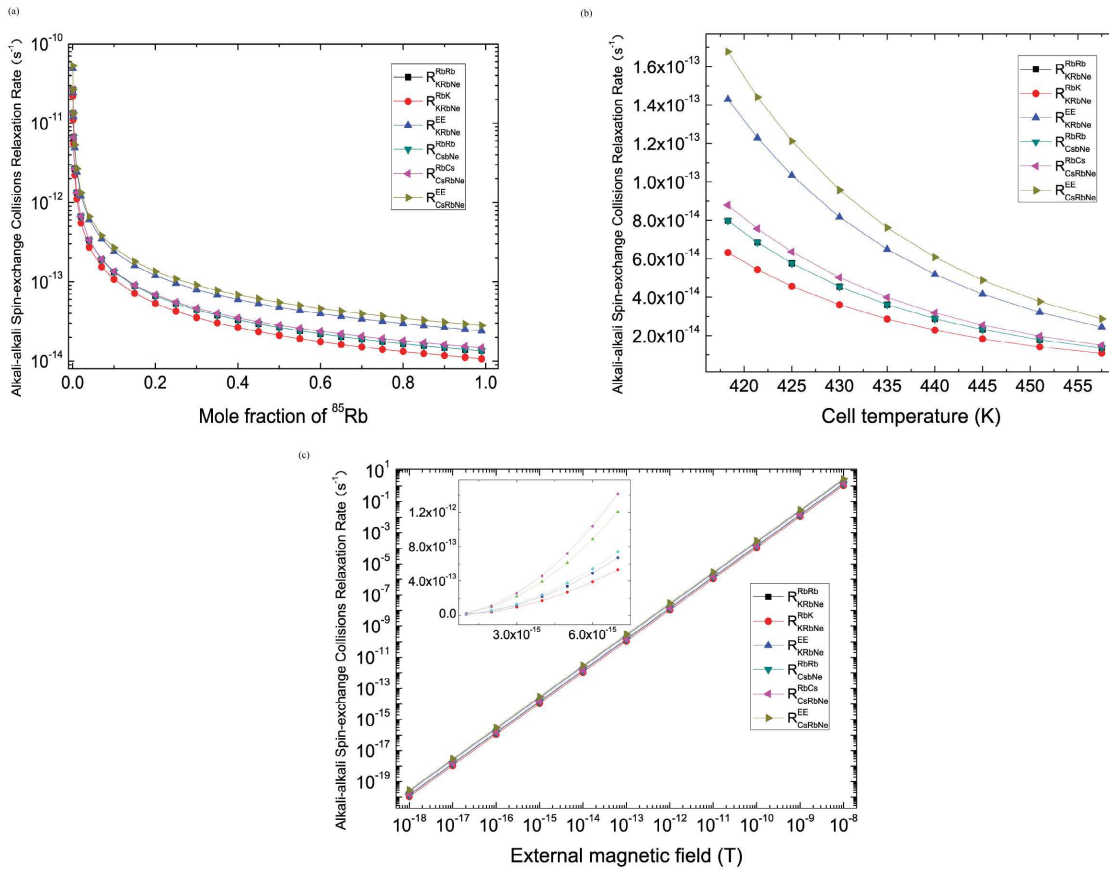
magnetometer respectively, then decreases in Fig. 11(c), which is caused by the pumping rate of the pump beam due to the pumping rate has the same pattern of change from Fig. 8(e). When the mole fraction of ^{85}Rb f_{Rb} is smaller than about 0.0318 in ^{39}K - ^{85}Rb - ^{21}Ne and 0.0135 in ^{133}Cs - ^{85}Rb - ^{21}Ne co-magnetometer respectively, B^e increases with the increasing f_{Rb} , otherwise, B^e decreases in Fig. 11(d). From the equation of B^e , P_{zRb}^e and M_0^{Rb} , we can know that M_0^{Rb} increases with the increasing f_{Rb} , P_{zRb}^e decreases when the f_{Rb} increases, hence, there is a biggest B^e when the B^e changes with the f_{Rb} .

B^e increase rapidly with the increasing photon number flux Φ_{D1} when the Φ_{D1} is smaller than about $5 \times 10^{24} \text{ s}^{-1}$ in ^{39}K - ^{85}Rb - ^{21}Ne and $3 \times 10^{25} \text{ s}^{-1}$ in ^{133}Cs - ^{85}Rb - ^{21}Ne co-magnetometer respectively, then increases slowly and tends to a constant in Fig. 12(a) due to only the pumping rate increases with the increasing Φ_{D1} in the equation of B^e and P_{zRb}^e , P_{zRb}^e has the same pattern of change, which makes the B^e have the change rule above. B^e increases when cell effective radius a increases in Fig. 12(b) duo to the increasing a decreases R_{wall}^{Rb} , which makes P_{zRb}^e increase so that the B^e increases with the increasing a .

B^e decreases when pump beam spot radius a_p increases with $a = 5\text{cm}$ in Fig. 12(c) duo to the increasing a_p makes the pumping rate decrease so that the P_{zRb}^e decreases, hence the B^e decreases with the increasing a_p . B^e increases with the increasing cell temperature T in Fig. 12(d). From the equation of B^e , P_{zRb}^e , R_{SD} , R_{wall}^{Rb} , M_0^{Rb} , Fig. 2(a) and Fig. 8(f), we can know that $R_{wall-K-Rb-Ne}^{Rb-Ne-N2}$, $R_{wall-Cs-Rb-Ne}^{Rb-Ne-N2}$, R_{SD} , M_0^{Rb} , R_p^K and R_p^{Cs} increase with the increasing T . We find that P_{zRb}^e decreases with the increasing T , but the increasing magnitude of M_0^{Rb} is bigger than

the decreasing magnitude of P_{zRb}^e , which makes B^e increase when T increases. Fig. 12(e) shows that B^e increases when the power density of pump beam I_{PI}^K and I_{PI}^{Cs} increase but is smaller than a critical value about $5.499 \times 10^5 \text{ W/cm}^2$ and $1.6156 \times 10^7 \text{ W/cm}^2$, respectively, otherwise, it will decrease.

The variations of the alkali-alkali spin-exchange collisions relaxation rate In this section, we calculated the variation of the alkali-alkali spin-exchange collisions relaxation rate related with ^{85}Rb atom changes with the mole fraction of ^{85}Rb f_{Rb} , the cell temperature T and the external magnetic field B .



The alkali-alkali spin exchange collisions relaxation rate related with ^{85}Rb atom changes with the mole fraction of ^{85}Rb in Fig. 13(a), the cell temperature in Fig. 13(b) and the external magnetic field in Fig. 13(c).

Fig. 13(a), Fig. 13(b) and Fig. 13(c) show that the ^{85}Rb - ^{39}K spin exchange collisions relaxation rate for ^{85}Rb - ^{39}K spin exchange collisions in ^{39}K - ^{85}Rb - ^{21}Ne co-magnetometer $R_{K\text{RbNe}}^{RbK}$, the ^{85}Rb - ^{133}Cs spin exchange collisions relaxation rate for ^{85}Rb - ^{133}Cs spin exchange collisions in ^{133}Cs - ^{85}Rb - ^{21}Ne co-magnetometer $R_{Cs\text{RbNe}}^{RbCs}$, the ^{85}Rb - ^{85}Rb spin-exchange collision relaxation rate for ^{85}Rb - ^{85}Rb spin exchange collisions in ^{39}K - ^{85}Rb - ^{21}Ne co-magnetometer $R_{K\text{RbNe}}^{RbRb}$, the ^{85}Rb - ^{85}Rb spin exchange collision relaxation rate for ^{85}Rb - ^{85}Rb spin exchange collisions in ^{133}Cs - ^{85}Rb - ^{21}Ne co-magnetometer $R_{Cs\text{RbNe}}^{RbRb}$, the sum of $R_{K\text{RbNe}}^{RbK}$ and $R_{K\text{RbNe}}^{RbRb}$ $R_{K\text{RbNe}}^{EE}$, the sum of $R_{Cs\text{RbNe}}^{RbCs}$ and $R_{Cs\text{RbNe}}^{RbRb}$ $R_{Cs\text{RbNe}}^{EE}$ decrease with the increasing f_{Rb} and T for the increasing f_{Rb} and T make spin transfer rate from ^{85}Rb to ^{39}K $R_{\text{Rb-K}}^{SE}$, from ^{85}Rb to ^{85}Rb $R_{\text{Rb-Rb}}^{SE}$ and from ^{85}Rb to ^{133}Cs $R_{\text{Rb-Cs}}^{SE}$ increase, which is inversely proportional to the $R_{K\text{RbNe}}^{RbK}$, $R_{K\text{RbNe}}^{RbRb}$, $R_{Cs\text{RbNe}}^{RbRb}$, $R_{Cs\text{RbNe}}^{RbCs}$ in equation (5), respectively. $R_{K\text{RbNe}}^{RbK}$, $R_{K\text{RbNe}}^{RbRb}$, $R_{Cs\text{RbNe}}^{RbRb}$, $R_{Cs\text{RbNe}}^{RbCs}$, $R_{K\text{RbNe}}^{EE}$, $R_{Cs\text{RbNe}}^{EE}$ increase with the B for the increasing B making the spin precession rate increase, which is proportional to the $R_{K\text{RbNe}}^{RbK}$, $R_{K\text{RbNe}}^{RbRb}$, $R_{Cs\text{RbNe}}^{RbRb}$, $R_{Cs\text{RbNe}}^{RbCs}$ in equation (5), respectively.

1. Schreiber, K. U. *et al.* How to detect the Chandler and the annual wobble of the Earth with a large ring laser gyroscope. *Phys. Rev. Lett.* **107**, 173904 (2011).
2. Schreiber, K. U. & Wells, J-P. R. Invited Review Article: Large ring lasers for rotation sensing. *Rev. Sci. Instrum.* **84**, 041101 (2013).
3. Shahriar, M. S. and Salit, M. Application of fast-light in gravitational wave detection with interferometers and resonators. *J. Mod. Opt.* **55**, 3133 (2008).
4. Stedman, G. E. Ring-laser tests of fundamental physics and geophysics. *Rep. Prog. Phys.* **60**, 615 (1997).
5. Everitt, C. W. F. *et al.* Gravity Probe B: Final Results of a Space Experiment to Test General Relativity. *Phys. Rev. Lett.* **106**, 221101 (2011).
6. Lefèvre, H. C. The fiber-optic gyroscope: Challenges to become the ultimate rotation-sensing technology. *Opt. Fiber Technol.* **19**, 828 (2013).
7. Kominis, I. K. *et al.* A subfemtotesla multichannel atomic magnetometer. *Nature* **422**, 596-599 (2003).
8. Kornack, T. W. Ghosh, R. K. & Romalis, M. V. Nuclear spin gyroscope based on an atomic comagnetometer. *Phys. Rev. Lett.* **95**, 230801 (2005).
9. Meyer, D. & Larsen, M. Nuclear magnetic resonance gyro for inertial navigation. *Gyroscopy Navigation* **5**, 75 (2014).

10. Brown, J. M. *et al.* New limit on Lorentz - and CPT - violating neutron spin interactions. *Phys. Rev. Lett.* **105**, 151604 (2010).
11. Smiciklas, M. *et al.* New Test of Local Lorentz Invariance Using a Ne²¹ - Rb - K Comagnetometer. *Phys. Rev. Lett.* **107**, 171604 (2011).
12. Vasilakis, G. *et al.* Limits on new long range nuclear spin-dependent forces set with a K-³He comagnetometer. *Phys. Rev. Lett.* **103**, 261801 (2009).
13. Tullney, K. *et al.* Constraints on spin-dependent short-range interaction between nucleons. *Phys. Rev. Lett.* **111**, 100801 (2013).
14. Bulatowicz, M. *et al.* A Laboratory Search for a Long-Range T-odd, P-odd Interaction from Axion-Like Particles using Dual Species Nuclear Magnetic Resonance with Polarized Xe¹²⁹ and Xe¹³¹ Gas. *Phys. Rev. Lett.* **111**, 102001 (2013).
15. Arvanitaki, A. & Geraci, A. A. Resonant detection of axion mediated forces with Nuclear Magnetic Resonance. *Phys. Rev. Lett.* **113**, 161801 (2014).
16. Rosenberry, M. A. & Chupp, T. E. Atomic Electric Dipole Moment Measurement Using Spin Exchange Pumped Masers of ¹²⁹Xe and ³He. *Phys. Rev. Lett.* **86**, 22 (2001).
17. Kornack, T. W. A test of CPT and Lorentz symmetry using a potassium-helium3 comagnetometer. *Princeton University* (2005).
18. Fang, J. C. *et al.* A novel Cs-¹²⁹Xe atomic spin gyroscope with closed-loop Faraday modulation. *Rev. Sci. Instrum.* **84**, 083108 (2013).

19. Zeng, X. *et al.* Experimental determination of the rate constants for spin exchange between optically pumped K, Rb, and Cs atoms and Xe^{129} nuclei in alkali-metal - noble-gas van der Waals molecules. *Phys. Rev. A* **31**, 260 (1985).
20. Jiang, L. W. *et al.* Suppression of the cross-talk effect in a dual-axis K-Rb- ^{21}Ne comagnetometer. *Phys. Rev. A* **95**, 062103 (2017).
21. Jiang, L. W. *et al.*, A parametrically modulated dual-axis atomic spin gyroscope. *Appl. Phys. Lett.* **112**, 054103 (2018).
22. Ito, Y. *et al.* Effect of Spatial Homogeneity of Spin Polarization on Magnetic Field Response of an Optically Pumped Atomic Magnetometer Using a Hybrid Cell of K and Rb Atoms. *IEEE T. Magn.* **48**, 3715-3718 (2012).
23. Romalis, M. V. Hybrid optical pumping of optically dense alkali-metal vapor without quenching gas. *Phys. Rev. Lett.* **105**, 243001 (2010).
24. J. H. Liu *et al.* The polarization and the fundamental sensitivity of $^{39}\text{K}(^{133}\text{Cs})\text{-}^{85}\text{Rb}\text{-}^4\text{He}$ hybrid optical pumping spin exchange relaxation free atomic magnetometers. *Sci. Rep.* **7**, 6776 (2017).
25. Alcock, C. B., Itkin, V. P. & Horrigan, M. K. Vapour Pressure Equations for the Metallic Elements: 298-2500 K. *Can. Metall. Quart.* **23**, 309-313 (1984).
26. Ito, Y., Sato, D., Kamada, K. & Kobayashi, T. Optimal densities of alkali metal atoms in an optically pumped K-Rb hybrid atomic magnetometer considering the spatial distribution of spin polarization. *Opt. Express* **24**, 015391 (2016).

27. Seltzer, S. J. Developments in Alkali-Metal Atomic Magnetometry. *Princeton University* (2008).
28. Happer, W. & Tam, A. C. Effect of rapid spin exchange on the magnetic-resonance spectrum of alkali vapors. *Phys. Rev. A* **16**, 1877-1891 (1977).
29. Dong, H. F., Xuan, L. F., Zhuo, C. & Lin, H. B. Two Unshielded SERF Magnetometer Schemes and Their Comparison. *J. Test Meas. Techol.* **26**, 468 (2012).
30. Babcock, E., Nelson, I., Kadlecek, S., Driehuys, B., Anderson, L. W., Hersman, F. W. & Walker, T. G. Hybrid Spin-Exchange Optical Pumping of ^3He . *Phys. Rev. Lett.* **91**, 123003 (2003).
31. Romalis, M. V., Miron, E. and Cates, G. D. Pressure broadening of Rb D1 and D2 lines by ^3He , ^4He , N_2 , and Xe: Line cores and near wings. *Phys. Rev. A* **56**, 4569 (1997).
32. Citron, M. L., Gray, H. R., Gabel, C. W. *et al.* Experimental study of power broadening in a two-level atom. *Phys. Rev. A* **16**, 1507 (1977).
33. Cole, H. R. & Olson, R. E. Spin-exchange cross sections for hydrogen-atom-alkali-metal-atom collisions. *Phys. Rev. A* **31**, 2137 (1985).
34. Fang, J. C., Wang, T., Zhang, H., Li, Y. & Zou, S. Optimizations of spin-exchange relaxation-free magnetometer based on potassium and rubidium hybrid optical pumping. *Rev. Sci. Instrum.* **85**, 123104 (2014).

35. Chen, Y., Quan, W., Duan, L. H., Lu, Y., Jiang, L. W. & Fang, J. C. Spin-exchange collision mixing of the K and Rb ac Stark shifts. *Phys. Rev. A* **94**, 052705 (2016).
36. Allred, J. C., Lyman, R. N., Kornack, T. W. & Romalis, M. V. High-sensitivity atomic magnetometer unaffected by spin-exchange relaxation. *Phys. Rev. Lett.* **89**, 130801 (2002).
37. Schaefer, S. R., Cates, G. D., Chien, Ting-Ray *et al.* Frequency shifts of the magnetic-resonance spectrum of mixtures of nuclear spin-polarized noble gases and vapors of spin-polarized alkali-metal atoms. *Phys. Rev. A* **39**, 5613 (1989).
38. Ghosh, R. K. & Romalis, M. V. Measurement of spin-exchange and relaxation parameters for polarizing ^{21}Ne with K and Rb. *Phys. Rev. A* **81**, 043415 (2010).
39. Franz, F. A. & Volk, C. Electronic spin relaxation of the $4^2\text{S}_{1/2}$ state of K induced by K-He and K-Ne collisions. *Phys. Rev. A* **26**, 85-92 (1982).
40. Franz, F. A. & Sooriamoorthi, C. E. Spin relaxation within the $6^2\text{P}_{1/2}$ and $6^2\text{S}_{1/2}$ states of cesium measured by white-light optical pumping. *Phys. Rev. A* **10**, 126-140 (1974).
41. Franz, F. A. & Volk, C. Spin relaxation of rubidium atoms in sudden and quasimolecular collisions with light-noble-gas atoms. *Phys. Rev. A* **14**, 1711-1728 (1976).
42. Silver, J. A. Measurement of atomic sodium and potassium diffusion coefficients. *J. Chem. Phys.* **81**, 5125-5130 (1984).
43. Fang, J. C., Chen, Y., Zou, S. *et al.*, Low frequency magnetic field suppression in an atomic spin co-magnetometer with a large electron magnetic field. *J. Phys. B* **49**, 065006 (2016).

44. Ledbetter, M. P., Savukov, I. M., Acosta, V. M., Budker, D. & Romalis, M. V. Spin-exchange-relaxation-free magnetometry with Cs vapor. *Phys. Rev. A* **77**, 033408 (2008).
45. Hager, G. D., Lott, G. E., Archibald, A. J. *et al.* High pressure line shapes for Cs D1 and D2 lines and empirically informed interaction potentials. *J. Quant. Spectrosc. Radiat. Transf.* **147**, 261-273 (2014).
46. Walker, T. G. & Happer, W. Spin-exchange optical pumping of noble-gas nuclei. *Rev. Mod. Phys.* **69**, 629-642 (1997).
47. Migdalek, J. & Kim, Y. -K. Journal of Physics B: Atomic, Molecular and Optical Physics Core polarization and oscillator strength ratio anomaly in potassium, rubidium and caesium. *J. Phys.* **31**, 1947-1960 (1998).
48. Caliebe, E. & Niemax, K. Oscillator strengths of the principal series lines of Rb. *J. Phys. B* **12**, L45 (1979).
49. Lwin, N. & McCartan, D. G. Collision broadening of the potassium resonance lines by noble gases. *J. Phys. B* **11**, 3841 (1978).
50. Appelt, A., Baranga, B. A., Erickson, C. J., Romalis, M. V., Young, A. R. & Happer, W. Theory of spin-exchange optical pumping of ^3He and ^{129}Xe . *Phys. Rev. A* **58**, 1412-1439 (1998).
51. Gibbs, H. M. & Hull, R. J. Spin-Exchange Cross Sections for $\text{Rb}^{87}\text{-Rb}^{87}$ and $\text{Rb}^{87}\text{-Cs}^{133}$ Collisions. *Phys. Rev.* **153**, 132-151 (1967).

52. Ressler, N. W., Sands, R. H. & Stark, T. E. Measurement of Spin-Exchange Cross Sections for Cs^{133} , Rb^{87} , Rb^{85} , K^{39} , and Na^{23} . *Phys. Rev.* **184**, 102-118 (1969).
53. Shao, W. J., Wang, G. D. & Hughes, E. W. Measurement of spin-exchange rate constants between ^{129}Xe and alkali metals. *Phys. Rev. A* **72**, 022713 (2005).
54. Quan, W., Li, Y. & Liu, B. Simultaneous measurement of magnetic field and inertia based on hybrid optical pumping. *Europhys. Lett.* **110**, 60002 (2015).
55. Aleksandrov, E. B., Balabas, M. V., Vershovskii, A. K., Okunevich, A. I. & Yakobson, N. N. Spin-exchange broadening of magnetic-resonance line of potassium atoms. *Opt. Spectrosc.* **87**, 329-334 (1999).
56. Franzen, W. Spin Relaxation of Optically Aligned Rubidium Vapor. *Phys. Rev.* **115**, 850-856 (1959).
57. Beverini, N., Minguzzi, P. & Strumia, F. Foreign-Gas-Induced Cesium Hyperfine Relaxation. *Phys. Rev. A* **5**, 993 (1972).
58. Kadlecik, S., Anderson, L. W. & Walker, T. Measurement of potassium-potassium spin relaxation cross sections. *Nucl. Instr. Meth. Phys. Res.* **402**, 208-211 (1998).
59. Fang, J. C. & Qin, J. Advances in Atomic Gyroscopes: A View from Inertial Navigation Applications. *Sensors* **12**, 6331-6346 (2012).
60. Fang, J. C., Li, R. J., Duan, L. H., Chen, Y. & Quan, W. Study of the operation temperature in the spin-exchange relaxation free magnetometer. *Rev. Sci. Instrum.* **86**, 073116 (2015).

61. Chen, Y., Quan, W., Zou, S., Lu, Y., Duan, L. H., Li, Y., Zhang, H., Ding, M. & Fang, J. C. Spin exchange broadening of magnetic resonance lines in a high-sensitivity rotating K-Rb- ^{21}Ne co-magnetometer. *Sci. Rep.* **6**, 36547 (2016).
62. Vliegen, E., Kadlecěk, S., Anderson, L. W., Walker, T. G., Erickson, C. J. & Happer, W. Faraday rotation density measurements of optically thick alkali metal vapors. *Nucl. Instrum. Methods Phys. Res. A* **460**, 444-450 (2001).
63. Bhaskar, N. D., Pietras, J., Camparo, J., Happer, W. & Liran, J. Spin Destruction in Collisions between Cesium Atoms. *Phys. Rev. Lett.* **44**, 930-933 (1980).
64. Dutta, I., Savoie, D., Fang, B. *et al.* Continuous cold-atom inertial sensor with 1 nrad/sec rotation stability. *Phys. Rev. Lett.* **116**, 183003 (2016).

Acknowledgement We thank P. S. He (Beijing Technology and Business University), Y. Chen (Harvard University), J. X. Lu (Beihang University), K. Wei (Beihang University), L. W. Jiang (Beihang University) for discussions and communications. This work was supported by the NKRDP under grants Nos. 2016YFA0301500, NSFC under grants Nos. 61405003, 11434015, 61227902, 61378017, 61835013, 11611530676, KZ201610005011, SKLQOQOD under grants No. KF201403, SPRPCAS under grants No. XDB01020300, XDB21030300.

Author Contributions J.H.L., W.Q. and W.M.L. proposed the ideas. J.H.L. interpreted physics, performed the theoretical as well as the numerical calculations and wrote the main manuscript. D.Y.J., L.Z., W.Q., J.C.F. and W.M.L. checked the calculations and the results. All of the authors reviewed the manuscript.

Competing Interests The authors declare that they have no competing interests as defined by Nature Research, or other interests that might be perceived to influence the results and/or discussion reported in this paper.

Correspondence Correspondence and requests for materials should be addressed to Wu-Ming Liu (email: wliu@iphy.ac.cn) and Wei Quan(quanwei@buaa.edu.cn).